



Article

# A Spectral/hp-Based Stabilized Solver with Emphasis on the Euler Equations

Rakesh Ranjan 1,2,\*, Lucia Catabriga 3 and Guillermo Araya 4,\*

- <sup>1</sup> Kord Technologies, 6200 Redstone Gateway, Huntsville, AL 35806, USA
- Department of Mechanical Engineering, University of Texas at San Antonio, San Antonio, TX 78249, USA
- Department of Informatic, Federal University of Espírito Santo, Av. Fernando Ferrari 514, Vitória 29075-910, Brazil; luciac@inf.ufes.br
- Computational Turbulence and Visualization Lab, Department of Mechanical Engineering, University of Texas at San Antonio, One UTSA Circle, San Antonio, TX 78249, USA
- \* Correspondence: rrakeshtamu@gmail.com (R.R.); araya@mailaps.org (G.A.)

**Abstract:** The solution of compressible flow equations is of interest with many aerospace engineering applications. Past literature has focused primarily on the solution of Computational Fluid Dynamics (CFD) problems with low-order finite element and finite volume methods. High-order methods are more the norm nowadays, in both a finite element and a finite volume setting. In this paper, inviscid compressible flow of an ideal gas is solved with high-order spectral/hp stabilized formulations using uniform high-order spectral element methods. The Euler equations are solved with high-order spectral element methods. Traditional definitions of stabilization parameters used in conjunction with traditional low-order bilinear Lagrange-based polynomials provide diffused results when applied to the high-order context. Thus, a revision of the definitions of the stabilization parameters was needed in a high-order spectral/hp framework. We introduce revised stabilization parameters,  $au_{supg}$ , with low-order finite element solutions. We also reexamine two standard definitions of the shock-capturing parameter,  $\delta$ : the first is described with entropy variables, and the other is the  $YZ\beta$ parameter. We focus on applications with the above introduced stabilization parameters and analyze an array of problems in the high-speed flow regime. We demonstrate spectral convergence for the Kovasznay flow problem in both  $L^1$  and  $L^2$  norms. We numerically validate the revised definitions of the stabilization parameter with Sod's shock and the oblique shock problems and compare the solutions with the exact solutions available in the literature. The high-order formulation is further extended to solve shock reflection and two-dimensional explosion problems. Following, we solve flow past a two-dimensional step at a Mach number of 3.0 and numerically validate the shock standoff distance with results obtained from NASA Overflow 2.2 code. Compressible flow computations with high-order spectral methods are found to perform satisfactorily for this supersonic inflow problem configuration. We extend the formulation to solve the implosion problem. Furthermore, we test the stabilization parameters on a complex flow configuration of AS-202 capsule analyzing the flight envelope. The proposed stabilization parameters have shown robustness, providing excellent results for both simple and complex geometries.

**Keywords:** high-order stabilization parameter; stabilized finite element; Euler equations; atmospheric reentry; supersonic flow; AS-202



Citation: Ranjan, R.; Catabriga, L.; Araya, G. A Spectral/hp-Based Stabilized Solver with Emphasis on the Euler Equations. *Fluids* **2024**, *9*, 18. https://doi.org/10.3390/fluids9010018

Academic Editors: Artur V. Dmitrenko and D. Andrew S. Rees

Received: 28 October 2023 Revised: 21 December 2023 Accepted: 30 December 2023 Published: 8 January 2024



Copyright: © 2024 by the authors. Licensee MDPI, Basel, Switzerland. This article is an open access article distributed under the terms and conditions of the Creative Commons Attribution (CC BY) license (https://creativecommons.org/licenses/by/4.0/).

## 1. Introduction

Initial efforts towards the development of solution procedures for problems in high-speed flight regimes involved the usage of Modified Newtonian methods with primary applications in the hypersonic regime with the main focus on atmospheric reentry systems. Later developments involved solving compressible flow equations with Computational Fluid Dynamics (CFD). Among the different CFD techniques available in the literature,

Fluids **2024**, 9, 18

we can mention flux-based procedures (finite difference and finite volume methods) and stabilized finite element methodologies. In the finite element community, Galerkin finite element methods were proposed to solve elliptic partial differential equations. With the well-known weaknesses of the Galerkin finite element methods for solving Navier-Stokes equations, various methods have been proposed to alleviate these difficulties. The methods that have gained acceptance are based on stabilized finite element methods [1–3]. Finite element methods have not had the same usage as finite volume methods for solving CFD problems because of the complexity of the variational formulation for compressible flow. Simpler weighted essentially nonoscillatory schemes (WENO) or essentially nonoscillatory (ENO) schemes provide a (high-order) interpolation scheme. Initial approximations of the inviscid fluxes are transformed to a curvilinear coordinate system following inverse trasformations [4,5]. In terms of computational expense, finite volume methods perform better because explicit schemes in conjunction with approximate Riemann solvers (flux approximations) obviate the need to solve a discrete system. Alternatively, line implicit methods can be used if an implicit approach is desired. Finite element methods, in comparison, have many advantages over other discretization schemes.

Finite element methods, in general, (1) are more amenable to complex discretizations and unstructured meshes, (2) do not require an interstencil construction of high-order approximations, (3) are not locally lower order near the limiters as are high-order finite volume schemes, and (4) have well-defined boundary conditions, not dependent on local metrics to transform the fluxes on the provided faces in a high-order context. Augmentation of incompressible flow formulation ASUPG and AGLS was first presented in a technical report by Ranjan [6] and formally in a paper by Ranjan et al. [7,8]. If one were to compare finite volume, spectral element methods, and finite element-based schemes, the coarse element counts that finite volume methods require provide a high competitive edge versus extensive refinements are required by low-order finite element methods. The coarse macro mesh, on the other hand, required by spectral methods, is a lot more competitive compared to the finite volume methods. In this paper, we discuss solving compressible flow equations with spectral/hp element methods. A historical perspective of the stabilized methods for compressible flow computations were provided by Hughes et al. [9] for the 25 years of research from themselves and their collaborators. Stabilized formulations are now used as a viable formulation for solving high-speed flow problems in high Mach number regimes. Stabilized finite element methods provide a variational framework for solving Euler equations. One of the main drawbacks of the low-order stabilized finite element methods is the localized mesh refinements required in regions where there are shock discontinuities or changes in the geometry. Large-scale low-order finite volume implementations also involve approximating the solution of Euler equations with some added artificial diffusion. High-order finite volume codes including NASA OverFlow [10] or Helios [11] often involve solving compressible flow equations with an interpolation scheme. This involves the construction of high-order interpolation stencils, which are more compact than a finite element low-order spatial discretization. Furthermore, the stencils span different finite volumes, which are constructed to appropriately model the flux at the interface. Some studies of FE based on the hpk framework [12,13] allowed higher-order global differentiability approximation and the variationally consistent integral forms, which guarantees unconditionally stable computations and does not require upwinding methods.

There is recent literature that addresses solutions of Euler equations. In the paper by Ibrahim [14], the limiting behavior of Riemann solutions to the Euler equations for compressible fluids in power law is studied as the adiabatic exponent goes to zero. They also provide some numerical results at the end of the paper. In a following paper, Ibrahim [15] explored the limiting behavior of Riemann solutions to the Euler equations in isentropic gas dynamics with general pressure law. In the paper by [16], they solved the piston problem constructively for one-dimensional isoentropic Euler equations of modified Chaplygin gas. In the solutions, they prove rigorously the global existence and uniqueness of a shock wave separating constant states ahead of the piston when the piston pushes forward into the gas.

Fluids **2024**, 9, 18 3 of 29

Some of the earlier work with hp adaptation was addressed in Oden et al. [17]. They solved the blunt body problem with cubic elements, with the classical artificial viscosity technique with Lapidus artificial viscosity due to Lohner et al. [18]. Spectral/hp element methods, on the other hand, provide the flexibility of obtaining highly accurate results on coarse macro meshes. An appropriate control on the polynomial expansion in each element provides the flexibility of working with the same macro mesh in an enriched hp space. Alternative methods to achieving stabilization within the spectral element framework have been approached via spectral filtering [19] and spectral viscosity [20,21].

Newly devised schemes that are *hpk* accurate with Nonuniform Rational B-spline interpolations (NURBS) have found extensive usage recently for solving problems in computational fluid dynamics (CFD) [22]. Alternative formulations with isogeometric finite elements have been applied to compressible flow computations in some recent work [23]. While the high-order isogeometric methods provide control on the *k* continuity on the space of solutions, there are some issues with diffusion of results because of noninterpolatory nature of b-splines and inaccuracies in boundary conditions enforcement. Spectral/hp element methods as an alternative provide spectrally accurate results at a minor loss of continuity requirement in the enriched hp element space. Spectral element methods have not found extensive applications in the CFD community within the framework of stabilized finite element technologies because of high quadrature requirements and supposed lack of enough resolution in the near vicinity of shock discontinuities in high-speed flow scenarios. Ranjan et al. [24] addressed the solution of high-order Navier-Stokes equations within the compressible flow regime. However, the previously mentioned article does not guarantee the intricate stability of the spectrally vanishing stabilization parameters for the Euler equations. Complex interactions with free slip boundary conditions enforcement cannot be ignored or assumed, and a distinct and new set of stabilization parameters are introduced, for solving problems with no viscous effects. To fill that research gap, an appropriate revision of stabilization parameters is performed in the present manuscript. We compare two stabilization parameters introduced and delineate the advantages of one parameter over the other in flow computations. In addition, to testing the revision of the stabilization parameters on the Euler equations, the present work also focuses on important applications.

In the following section, we describe the governing compressible flow equations in conservative variables, followed by a discussion of the basis utilized for approximating the primary variables. We highlight the details of stabilized finite element formulation in the following section. Following, we provide numerical solutions for benchmark problems that are described by Euler flow. Finally, we discuss conclusions and outline possible extensions of the work in the context of turbulence models.

### 2. Governing Equations

The governing equations for high-speed flow in the high Mach regime can be described by the inviscid Euler Equations [25–27]. Several applications of the Euler equations in fluid dynamics were described in review papers: computer simulations of fluid flow [28], CFD of the whole-body aircraft [29], tsunami simulations [30], and high-speed flows [31], just to name a few. In the absence of considerations of vibrational relaxation and for flows in vibrational-translational equilibrium, the conservative variables are defined as  $\mathbf{U} = (\rho, \rho u_1, \rho u_2, \rho e)$ :

$$\frac{\partial \mathbf{U}}{\partial t} + \frac{\partial \mathbf{F}_1}{\partial x} + \frac{\partial \mathbf{F}_2}{\partial y} = 0 \text{ on } \Omega \times [0, T]$$
 (1)

where  $\mathbf{F}_1$  and  $\mathbf{F}_2$  are the Euler fluxes, defined by:

$$\mathbf{F}_{1} = \left\{ \begin{array}{c} \rho u_{1} \\ \rho u_{1}^{2} + p \\ \rho u_{2} u_{1} \\ \rho H u_{1} \end{array} \right\} \qquad \mathbf{F}_{2} = \left\{ \begin{array}{c} \rho u_{2} \\ \rho u_{1} u_{2} \\ \rho u_{2}^{2} + p \\ \rho H u_{2} \end{array} \right\}$$
(2)

Fluids **2024**, 9, 18 4 of 29

where  $\rho$  is the fluid density,  $\mathbf{u}=(u_1,u_2)$  is the velocity vector, e is the total energy per unit mass, p is pressure, and  $H=e+\frac{p}{\rho}$ . Moreover,  $\Omega$  is the domain in  $R^2$  and T is a positive real number. We denote the spatial coordinates, respectively,  $\mathbf{x}=(x,y)\in\bar{\Omega}$  and  $t\in[0,T)$ , where the superimposed bar denotes set closure and  $\Gamma$  denotes the boundary of the domain  $\Omega$ . We consider an ideal gas for analysis. The equations are the first-order hyperbolic Euler equations without consideration of any viscous effects. Details regarding the mathematical model of the Euler Equations can be found in [32].

Introducing the inviscid Jacobian matrices, we can express the above set of equations as:

$$\frac{\partial \mathbf{U}}{\partial t} + \mathbf{A}_1 \frac{\partial \mathbf{U}}{\partial x} + \mathbf{A}_2 \frac{\partial \mathbf{U}}{\partial y} = 0 \text{ on } \Omega \times [0, T]$$
(3)

where  $A_1 = \frac{\partial F_1}{\partial U}$  and  $A_2 = \frac{\partial F_2}{\partial U}$  are the Jacobian matrices. The specification of the ideal gas state equation and prescription of the boundary and initial conditions provide a complete set of equations to be solved in the formulation. In the next section, we discuss the approximation with spectral/hp basis utilized for constructing the weighted residual statements of the compressible flow equations.

# 3. Spectral/hp Approximation

We introduce a new set of spectral basis that is utilized for approximating the set of Euler equations. The spectral finite element approximation is described as follows in one dimension. The conservative variables are approximated as follows:

$$\rho = \sum_{j=1}^{n} \rho_j \psi_j, \quad \rho u = \sum_{j=1}^{n} \rho u_j \psi_j$$

$$\rho v = \sum_{j=1}^{n} \rho v_j \psi_j, \quad \rho e = \sum_{j=1}^{n} \rho e_j \psi_j$$
(4)

where  $\psi_j$  are the nodal expansions, which are provided by the following one-dimensional  $C^0$  spectral nodal basis [33]:

$$\psi_i(\xi) = h_i^e(\xi) = \frac{(\xi - 1)(\xi + 1)L_n'(\xi)}{n(n+1)L_n(\xi_i)(\xi - \xi_i)}$$
(5)

In Equation (4),  $(\rho_j, \rho u_j, \rho v_j, \rho e_j)$  are the nodal values due to the Kronecker delta property of the spectral basis.  $L_n = P_n^{(0,0)}$  is the Legendre polynomial of order n and  $\xi_i$  denote the location of the roots of  $(\xi-1)(\xi+1)L_n'(\xi)=0$  in the interval [-1,+1]. The element matrices (derived in the following section) are obtained based on the Gauss–Lobatto–Legendre (GLL) rules, which include both endpoints of the interval, that is,  $\xi_i=\pm 1$ . The points and weights are, respectively, listed as:

$$\xi_{i} = \begin{cases} -1 & \text{if } i = 0, \\ \xi_{i-1,Q-2}^{1,1} & \text{if } i = 1, \dots, Q - 2 \\ 1 & \text{if } i = Q - 1 > 0. \end{cases}$$
 (6)

where Q is the number of quadrature points in the interval and  $\xi_{i,m}^{\alpha,\beta}$  are the roots of the Jacobi polynomial, which typically do not have an analytical form and are often tabulated. The running index i is the index that spans the quadrature points for the specific interval of interest.

The weights for the GLL quadrature rule are obtained as follows:

$$w_i^{0,0} = \frac{2}{Q(Q-1)[L_{Q-1}(\xi_i)]^2} \quad i = 0, 1, \dots, Q-1$$
 (7)

Fluids **2024**, 9, 18 5 of 29

where  $L_Q(\xi)$  is the Legendre polynomial given by  $L_Q(\xi) = P_Q^{0,0}(\xi)$ . First derivatives of the Legendre polynomials are required in the formulation. The first derivative differentiation matrix is provided as:

$$d_{ij} = \begin{cases} -\frac{Q(Q-1)}{4} & \text{if } i = j = 0, \\ \frac{L_{Q-1}(\xi_i)}{L_{Q-1}(\xi_j)} \frac{1}{(\xi_i - \xi_j)} & i \neq j, 0 \leq i, j \leq Q - 1 \\ 0 & \text{if } 1 \leq i = j \leq Q - 2, \\ \frac{Q(Q-1)}{4} & \text{if } i = j = Q - 1 \end{cases}$$
(8)

The differentiation operation utilizing the differentiation matrix is obtained by:

$$\frac{d}{dx}(\rho_j, \rho u_j, \rho v_j, \rho e_j) = \sum_{i=1}^n d_{ij}(\rho_j, \rho u_j, \rho v_j, \rho e_j)$$
(9)

The construction of the two-dimensional spectral basis follows a tensor product with nodal expansions in either direction. Thus, the construction of the tensor product follows:

$$\phi_{ij}(\xi_1, \xi_2) = \psi_i(\xi_1)\psi_i(\xi_2) \tag{10}$$

The above functions are defined locally to each spectral element  $\Omega_e$ . They are transformed into physical space with appropriate affine mapping:

$$\bar{\Omega} = \{ (\xi_1, \xi_2), -1 \le \xi_1, \xi_2 \le 1 \} \tag{11}$$

Extensions of these ideas to triangular elements have to follow the above definitions. The Gauss–Lobatto–Legendre (GLL) point locations along the sides of a generic triangle, along with generic formulae for the shape functions in triangular regions, provide an expression of the shape functions in area coordinates. Expressions in terms of area coordinates are standard for defining the high-order shape functions in triangular regions. Similar tensor product extensions in hexahedral elements and expressions in volume coordinates for tetrahedral complete the suite of high-order spectral expansions in three-dimensional regions.

## 4. Finite Element Formulation

In the following section, we describe the stabilized finite element formulation for solving Euler equations. The formulation admits the conservative formulation for the Euler equations with the primary variables as  $(\rho, \rho u, \rho v, \rho e)$ .

# 4.1. Stabilized Finite Element

In the process of development of the stabilized finite element formulation, we add conjugate terms to the test function  $\mathbf{W}^{hp}$ . This is the essence of the Streamline Upwind Petrov–Galerkin (SUPG) formulation as another stabilization mechanism for convection-dominated flows. Furthermore, the SUPG method has been used in cardiovascular flow simulations [34] and in unstructured meshes [35]. An intricate balance of the stabilization parameter in conjunction with the formulation ameliorates the oscillations inherent in the Galerkin finite element formulation. For the Euler equations, the method can be described by augmenting the Galerkin test function  $\mathbf{W}^{hp}$  with a convection operator acting on the test function [36]:

$$\hat{\mathbf{W}}^{hp} = \mathbf{W}^{hp} + \tau_{supg}^{hp} \left( \mathbf{A}_{1}^{hp} \frac{\partial \mathbf{W}^{hp}}{\partial x} + \mathbf{A}_{2}^{hp} \frac{\partial \mathbf{W}^{hp}}{\partial y} \right)$$
(12)

where,  $\tau_{supg}^{hp}$  is a diagonal stabilization matrix that will be defined in Section 4.2.

Fluids **2024**, 9, 18 6 of 29

Considering a standard discretization of  $\Omega$  into finite elements, the SUPG formulation for the Euler equations in conservative variables introduced in [3] supplemented with a shock-capturing term is written as in [37]:

$$\int_{\Omega} \left[ \mathbf{W}^{hp} \cdot \left( \frac{\partial \mathbf{U}^{hp}}{\partial t} + \mathbf{A}_{1}^{hp} \frac{\partial \mathbf{U}^{hp}}{\partial x} + \mathbf{A}_{2}^{hp} \frac{\partial \mathbf{U}^{hp}}{\partial y} \right) \right] d\Omega + \\
\sum_{e=1}^{n_{el}} \tau_{supg}^{hp} \int_{\Omega_{e}} \left( \frac{\partial \mathbf{W}^{hp}}{\partial x} \mathbf{A}_{1}^{hp} + \frac{\partial \mathbf{W}^{hp}}{\partial y} \mathbf{A}_{2}^{hp} \right) \cdot \\
\left( \frac{\partial \mathbf{U}^{hp}}{\partial t} + \mathbf{A}_{1}^{hp} \frac{\partial \mathbf{U}^{hp}}{\partial x} + \mathbf{A}_{2}^{hp} \frac{\partial \mathbf{U}^{hp}}{\partial y} \right) d\Omega_{e} + \\
\sum_{e=1}^{n_{el}} \delta^{hp} \int_{\Omega_{e}} \left( \frac{\partial \mathbf{W}^{hp}}{\partial x} \frac{\partial \mathbf{U}^{hp}}{\partial x} + \frac{\partial \mathbf{W}^{hp}}{\partial y} \frac{\partial \mathbf{U}^{hp}}{\partial y} \right) d\Omega_{e} = 0.$$
(13)

where  $\delta^{hp}$  is the shock capturing parameter [38], which is further discussed in the next section. Here,  $\mathbf{W}^{hp}$  and  $\mathbf{U}^{hp}$  are test and trial functions. In the variational formulation above, the first integral corresponds to the Galerkin formulation, the first series of element-level integrals are the SUPG stabilization terms, and the second series of element-level integrals are the shock capturing terms that are added to the variational formulation to prevent spurious oscillations around shocks.

We consider the following element-level matrices as defined in [39]:

$$\mathbf{m} := \int_{\Omega} \left( \mathbf{W}^{hp} \frac{\partial \mathbf{U}^{hp}}{\partial t} \right) d\Omega$$

$$\mathbf{k} := \int_{\Omega} \left( \mathbf{W}^{hp} \cdot \mathbf{A}_{1}^{hp} \frac{\partial \mathbf{U}^{hp}}{\partial x} \right) +$$

$$\left( \mathbf{W}^{hp} \cdot \mathbf{A}_{2}^{hp} \frac{\partial \mathbf{U}^{hp}}{\partial y} \right) d\Omega$$

$$\hat{\mathbf{k}}_{supg} := \int_{\Omega_{e}} \tau_{supg}^{hp} \left( \frac{\partial \mathbf{W}^{hp}}{\partial x} \cdot \mathbf{A}_{1}^{hp} \mathbf{A}_{1}^{hp} \frac{\partial \mathbf{U}^{hp}}{\partial x} \right) +$$

$$\tau_{supg}^{hp} \left( \frac{\partial \mathbf{W}^{hp}}{\partial x} \cdot \mathbf{A}_{1}^{hp} \mathbf{A}_{2}^{hp} \frac{\partial \mathbf{U}^{hp}}{\partial y} \right) +$$

$$\tau_{supg}^{hp} \left( \frac{\partial \mathbf{W}^{hp}}{\partial y} \cdot \mathbf{A}_{2}^{hp} \mathbf{A}_{1}^{hp} \frac{\partial \mathbf{U}^{hp}}{\partial x} \right) +$$

$$\tau_{supg}^{hp} \left( \frac{\partial \mathbf{W}^{hp}}{\partial y} \cdot \mathbf{A}_{2}^{hp} \mathbf{A}_{2}^{hp} \frac{\partial \mathbf{U}^{hp}}{\partial y} \right) d\Omega_{e}$$

$$\hat{\mathbf{k}}_{supg} := \int_{\Omega_{e}} \tau_{supg}^{hp} \left( \frac{\partial \mathbf{W}^{hp}}{\partial x} \cdot \mathbf{A}_{1}^{hp} \frac{\partial \mathbf{U}^{hp}}{\partial t} + \frac{\partial \mathbf{W}^{hp}}{\partial y} \cdot \mathbf{A}_{2}^{hp} \frac{\partial \mathbf{U}^{hp}}{\partial t} \right) d\Omega_{e}$$

$$\hat{\mathbf{k}}_{sc} := \delta^{hp} \int_{\Omega_{e}} \left( \frac{\partial \mathbf{W}^{hp}}{\partial x} \cdot \mathbf{A}_{1}^{hp} \frac{\partial \mathbf{U}^{hp}}{\partial x} + \frac{\partial \mathbf{W}^{hp}}{\partial y} \frac{\partial \mathbf{U}^{hp}}{\partial y} \right) d\Omega_{e}$$

$$(14)$$

The above definitions of matrices comprise the stabilized finite element formulation. Global operators (matrices and residuals) need to be assembled from the above local (element) matrices to complete the formulation. An important step in the formulation is defining the stabilization parameters, as they greatly affect the accuracy of the formulation.

In our numerical experiments, low-order finite element-based stabilization parameters were found to provide inaccurate results. We revise the definitions of stabilization parameters specific to spectral element methods that provide both stable and accurate

Fluids **2024**, 9, 18 7 of 29

temporal integration schemes for obtaining benchmark results for problems of interest in high speed computations. Furthermore, we revise the earlier definitions of the stabilization parameter within the context of the transformation from conservative variables to entropy variables [40] and the  $YZ\beta$  parameters separately [41]. The definitions of the stabilization parameters obviate the need to resort to collocation finite element procedures by using a single integration point in the evaluation of the element matrices with standard compressible flow finite element formulations. Usage of a single integration point collocation-based approach has been used in least squares finite element also to artificially reduce the effectivity index and obtain reasonable results for sample problems [42]. These ad hoc approaches seem to work well with lower-order finite element approximations; however, the usage of high-order polynomial approximations provide excessive diffusion in the formulation, as was noted when used for these approaches. In contrast, we utilized a full integration procedure without resorting to any ad hoc approaches for solving the Euler equations and obtain excellent agreement with benchmark results for problems.

## 4.2. High-Order Stabilization Parameter

The  $\tau_{supg}^{hp}$  and  $\delta^{hp}$  Equations (13) and (14) are both stabilization parameters present in the formulation. An appropriate revision of these parameters ultimately leads to accurate spectral schemes in compressible flow computations. Conceptually,  $\tau$  is a matrix of intrinsic time scales associated with the discrete solution [43], and unfortunately, the solution is strongly dependent on this choice [44]. Some developments in the stabilized finite element community has addressed solving Euler equations with a matrix  $\tau$ . A diagonal  $\tau$  has also been extensively studied in the literature [45]. Many applications of a diagonal  $\tau$  have been proven to provide excellent results with applications in both high Mach number flows [39] and further with considerations of nonequilibrium effects [36,44,46]. We revise the current definition of these parameters within the framework of a spectrally accurate stabilized finite element technology.

The first parameter in consideration is the streamline upwind Petrov Galerkin parameter. This parameter is defined as:

$$\tau_{\rho} = \tau_{\rho u} = \tau_{\rho v} = \tau_{\rho e} = \kappa \delta_{ij} \tau_{ij} \tag{15}$$

where  $\delta_{ij}$  is an appropriate contraction operator, specifically, the Kronecker delta. The expression for  $\kappa$  is defined utilizing the  $\prod_{\alpha}$  norm:

$$\kappa = \frac{\partial \xi_k}{\partial x_i}^{\gamma} \frac{\partial \eta_k}{\partial x_j}^{\gamma} \tag{16}$$

We consider values of the parameter  $\gamma = 4$ . Stabilization parameter  $\tau_{ii}$  is specified as a diagonal matrix as:

$$\tau_{ii} = \left[ \frac{1}{\tau_{sugn1}^{r}} + \frac{1}{\tau_{sugn2}^{r}} \right]^{-1/r}$$
 (17)

In the above formulae, the parameters  $\tau_{sugn1}$  and  $\tau_{sugn2}$  are defined as below:

$$\tau_{sugn1}^{\rho} = \tau_{sugn1}^{\mathbf{u}} = \tau_{sugn1}^{e} = \left(\sum_{a=1}^{n_{en}} \left(c\|\mathbf{j} \cdot \nabla N_{a}^{hp}\| + \|\mathbf{u}^{hp} \cdot \nabla N_{a}^{hp}\|\right)\right)^{-1}$$

$$(18)$$

Thus, the second component of the parameter is defined:

$$\tau^{\rho}_{sugn2} = \tau^{\mathbf{u}}_{sugn2} = \tau^{e}_{sugn2} = \frac{\Delta t}{2}$$
 (19)

Fluids **2024**, 9, 18 8 of 29

where  $\Delta t$  denotes the time step increment used and c denotes the speed of sound. We consider a value of r=2. The characteristic length of the macro spectral element is defined as:

$$h_{rgn} = 2 \left( \sum_{a=1}^{n_{en}} \| \mathbf{r} \cdot \nabla N_a \| \right)^{-1}$$
 (20)

where  $N_a$  is the interpolation for the spectral macro mesh utilized in the discretization of the problem and  $\bf r$  is defined as:

$$\mathbf{r} = \frac{\nabla \|\mathbf{u}^{hp}\|}{\|\nabla \|\mathbf{u}^{hp}\|\|} \tag{21}$$

In the present manuscript, we have introduced new definitions of the  $\tau^{hp}$  compared to definitions introduced in [24], whereas the definitions of the shock-capturing term remain as in [24]. Spectral convergence of the  $L^2$  error for incompressible flow computations provided some of the earliest insight into the definitions of the parameters in the high-order context. Furthermore, an insight into the more precise nonlinear convergence of the formulation introduced provides mathematical quantification into earlier ideas on multiscale effects in the context of incompressible flow computations.

The shock-capturing parameter,  $\delta^{\bar{h}p}$ , was adapted for a system of conservative variables by Aliabadi [47], Aliabadi and Tezduyar [48], and LeBeau [49] from the original definition employed by Hughes et al. [40] and Shakib et al. [43] for the case of entropy variables. A modified form is defined in this work as:

$$\delta^{hp} = \|g_{ij}\|_{\Pi_{\alpha}} \left[ \frac{\mathbf{A}_1 \frac{\partial \mathbf{U}^{hp}}{\partial x}^2 + \mathbf{A}_2 \frac{\partial \mathbf{U}^{hp}}{\partial y}^2}_{\mathbf{A}_0^{-1}} \right]^{\frac{1}{2}}$$

$$(22)$$

where  $(\xi, \eta)$  are the reference element normalized coordinates and  $\mathbf{A_0}^{-1}$  is the mapping from the conservative to entropy variables. The vector norm  $\mathbf{v_{A_0}^{-1}}$  is defined as  $[\mathbf{v^T}(\mathbf{A_0}^{-1}\mathbf{v})]$ . In the above equations,  $g_{ij}$  is the covariant metric tensor given by:

$$g_{ij} = \frac{\partial \xi_k}{\partial x_i} \frac{\partial \eta_k}{\partial x_i} \tag{23}$$

and the  $\prod_{\alpha}$  norm of the covariant matrix is defined as:

$$g_{ij}_{\Pi\alpha} = \frac{\partial \xi_k}{\partial x_i}^{\alpha} \frac{\partial \eta_k}{\partial x_j}^{\alpha} \tag{24}$$

where  $\alpha$  is chosen to be equal to 2. The parameters  $\xi$  and  $\eta$  denote the local coordinates defined on the master element. The above definitions introduced in this work, for the stabilization parameter for high-order elements, improves the accuracy of the formulation and also paves the way for a multiscale formulation for compressible flow. The reason for the introduction of the new definitions of the shock capturing parameters is the traditionally utilized definitions of the stabilization parameters provide diffused results in a high-order context. An example problem for providing the solution of the Carter plate problem has been provided in Ranjan et al. [24].

As a next step, we revise the definition of  $YZ\beta$  parameters proposed by Tezduyar et al. [41,50]. The revised  $YZ\beta$  can be written as:

$$\delta_{YZ\beta}^{hp} = g_{ij}_{\prod_{\alpha}} \|\mathbf{Y}^{-1}\mathbf{Z}\| \left( \sum_{i=1}^{n_{sd}} \mathbf{Y}^{-1} \frac{\partial \mathbf{U}^{2}}{\partial x_{i}} \right)^{\beta/2-1} \left( \frac{h_{shock}}{2} \right)^{\beta}$$
 (25)

Fluids **2024**, 9, 18 9 of 29

In the above equation, the characteristic element length is taken as the equivalent length of the spectral macro element. Here,  $\mathbf{Y}$  is a diagonal scaling matrix constructed from the reference values of the components of  $\mathbf{U}$  and  $h_{shock}$  refers to the characteristic element length for the spectral macro element used in the discretization.

$$\mathbf{Y}_{ij} = \delta_{ij} U_{r_{ij}} \tag{26}$$

The reference values of conservative variables  $U_r$  are usually taken as the free stream values of the conservative variables. The vector **Z** is defined as below:

$$\mathbf{Z} = \frac{\partial \mathbf{U}}{\partial t} + \mathbf{A}_1 \frac{\partial \mathbf{U}}{\partial x} + \mathbf{A}_2 \frac{\partial \mathbf{U}}{\partial y}$$
 (27)

The parameter  $\beta$  is set as a switch to 1.0 for smoother shocks and 2.0 for sharper shocks. For compressible flow computations, an averaging of the expression is often utilized [50]:

$$\delta_{YZ\beta}^{hp} = \frac{1}{2} \left( \delta_{YZ\beta,\beta=1}^{hp} + \delta_{YZ\beta,\beta=2}^{hp} \right)$$
 (28)

We use the expression for the  $\delta^{hp}$  and  $\delta^{hp}_{YZ\beta}$  introduced and test the new definitions on several problems involving the solution of Euler equations. The current definition of stabilization parameter does not require trial and error for every new problem. Some of the earlier work on this is in references by Bento et al. [51,52], which highlights a multiscale approach within the framework of stabilized finite element technology. These can be used as guiding principles to obtain more accurate results for high-order implementations. The current framework, via the definitions of the stabilization parameters, refers to achieving a true multiscale effect with both  $\tau^{hp}$  and  $\delta^{hp}$ . This brings ideas of a variational multiscale framework to compressible flow computations.

We establish spectral convergence with the new definitions of the stabilization parameters for a example with exact solution in both the  $L^1$  and  $L^2$  norms. With spectral convergence, it is implied that the solutions obtained from the computational framework developed converge to known analytical solutions to the Navier–Stokes equations exponentially. We provide below the definitions of the discrete form of  $L^1$  and  $L^2$  norms for a conservative variable q as follows:

$$L_1(q) = \frac{\sum_{i}^{N} |q|}{N}$$
  $L_2(q) = \sqrt{\frac{\sum_{i}^{N} ||q||^2}{N}}$  (29)

An appropriate representation for the errors requires subtracting the numerical solution from the analytical solutions to complete these definitions. In the above definitions, |q| is the absolute value of the variable and ||q|| is the norm of the variable q. Then, the high-order implementation for the solver is tested against exact solutions for Navier–Stokes equations.

## 4.3. Temporal Evolution

There are various strategies available for integration in time for the above set of equations. Among the schemes available are the explicit Runge–Kutta schemes for temporal evolution. We resort to the implicit method in the predictor–corrector algorithm. Spatial discretization of the governing partial differential equation leads to the problem of finding solutions for the equation below:

$$\mathbf{Ma} + \mathbf{K}(\mathbf{v})\mathbf{v} = 0 \tag{30}$$

where  $\mathbf{v}$  is the nodal values of  $\mathbf{U}^{hp}$ ,  $\mathbf{a}$  is the time derivative of  $\mathbf{v}$ ,  $\mathbf{M}$  is the generalized mass matrix obtained from local matrices  $\mathbf{m}$  and  $\hat{\mathbf{m}}_{supg}$  (Equations (13) and (14)), and  $\mathbf{K}(\mathbf{v})$  is the operator denoting all terms other than that comprising the mass matrix obtained from local

Fluids **2024**, 9, 18 10 of 29

matrices  $\mathbf{k}$ ,  $\hat{\mathbf{k}}_{supg}$ , and  $\mathbf{k}_{sc}$  in Equation (14). We utilize a high-order spectral discretization of the problem with node-based Legendre expansions, which automatically provides a diagonal mass matrix. We utilized a time implicit stepping algorithm. Specifically, we employ an implicit predictor multicorrector algorithm for long-term integration of the above differential equations. More details on the predictor multi-corrector algorithm can be found in Hughes and Tezduyar [2]. At each multicorrection step, one has to solve the following nonsymmetric equations:

$$\mathbf{M}^* \, \Delta \mathbf{a} = \mathbf{R}. \tag{31}$$

where  $\mathbf{M}^* = \mathbf{M} + \zeta \Delta t \mathbf{K}$ ,  $\mathbf{R}$  is the residual vector defined as  $\mathbf{R} = -\mathbf{M}\mathbf{a}^* - \mathbf{K}\mathbf{v}^*$ , and  $\Delta \mathbf{a}$  is the correction in the nodal values of  $\mathbf{a}$  from one nonlinear iteration to the next. We utilize the values of  $\zeta = 1$ , which provide a fully implicit first-order algorithm.

## 5. Numerical Examples

In this section, we first show the convergence rates of the Kovasznay flow in both the  $L^1$  and  $L^2$  norms. We also solve the Sod's shock, oblique shock, and reflected shock problems. Following these examples, we solve the two-dimensional blast wave and inviscid flow past a step at Mach number 3.0 and flow past an AS202 capsule at Mach 7.0. We utilize a single multi-correction for the problem solution. No preconditioning strategies were utilized for solving the linear system. Linear convergence was declared once the  $L^2$  residual is reduced by six orders of magnitude as compared to the initial residual.

#### 5.1. Kovasznay Flow

The Kovasznay fluid flow [53] is an exact solution of the Navier–Stokes (NS) equations, which somehow depicts the flow behind a two-dimensional grid. It is commonly used to validate numerical codes in solving two-dimensional NS equations in the low Mach regime (incompressible flow). Let the density of the Newtonian fluid be denoted by  $\rho$  and viscosity by  $\mu$ . Let the spatial computational domain be denoted by  $\Omega \subset R^N$ . The problem is described as a temporal evolution with the time  $t \in [0,T]$ . Let N denote the space dimension over which the problem is described. We denote the boundary as  $\Gamma$  for the computational domain of  $\Omega$ . The Navier–Stokes equations are specified below:

$$\frac{\partial \mathbf{u}}{\partial t} + \mathbf{u} \cdot \nabla \mathbf{u} + \nabla p - \frac{1}{Re} \nabla^2 \mathbf{u} = \mathbf{f} \text{ on } \Omega \,\forall \, t \in [0, T]$$
(32)

$$\nabla \cdot \mathbf{u} = 0, \text{ on } \Omega \,\forall \, t \in [0, T] \tag{33}$$

where  $\mathbf{u}$ , p, and  $\mathbf{f}$ , are the velocity, pressure, and gravitational force, respectively, the Reynolds number is denoted by Re,  $v = \frac{\mu}{\rho}$  is the kinematic viscosity, p denotes the pressure field, and  $\mathbf{u}$  denotes the velocity field. Let a subcomponent of the whole boundary  $\Gamma$  be partitioned into the part where velocity specifications have been made as  $\Gamma_g$ :

$$\mathbf{u} = \mathbf{g} \text{ on } \Gamma_{g} \ \forall t \in [0, T] \tag{34}$$

Spectral convergence with the new stabilization parameters introduced is established for the Kovasznay flow problem in both  $L^1$  and  $L^2$  norms. We examine the two-dimensional problem at a Reynolds number equal to 20 [53]. While the focus of the present article is on the inviscid Euler equations, by solving the viscous NS equations, the robustness of the proposed numerical approach is demonstrated. The analytical solutions are provided by [53].

The description of the problem requires us to consider a two-dimensional domain  $\Omega = [-0.5, 1.5] \times [-0.5, 1.5]$ . Kovasznay [53] provided analytical solutions to the problem as follows:

Fluids **2024**, 9, 18 11 of 29

$$u(x,y) = 1 - e^{\lambda x} \cos(2\pi y)$$

$$v(x,y) = \frac{\lambda}{2\pi} e^{\lambda x} \sin(2\pi y)$$

$$p(x,y) = p_0 - \frac{1}{2} e^{2\lambda x}$$
(35)

where  $\lambda = Re/2 - (Re^2/4 - 4\pi^2)^{1/2}$  and  $p_0$  is the reference pressure (an arbitrary constant). We consider value of the constant  $p_0 = 0.5$ . The problem requires specifying the set of boundary conditions to complete the problem description. To this end, we qualify the analytical solutions that describe the whole flow physics with the equations above to the boundaries. These restricted fields serve as the boundary conditions for the problem. Specifically, the following boundary conditions were applied:

Top Boundary:

$$u(x,y) = 1 + e^{\lambda x} \tag{36}$$

$$v(x,y) = 0 (37)$$

**Bottom Boundary:** 

$$u(x,y) = 1 + e^{\lambda x} \tag{38}$$

$$v(x,y) = 0 (39)$$

Left Boundary:

$$u(x,y) = 1 - e^{(-\lambda/2)}\cos(2\pi y) \tag{40}$$

$$v(x,y) = \frac{\lambda}{2\pi} e^{(-\lambda/2)} \sin(2\pi y) \tag{41}$$

$$p(x,y) = \frac{1}{2} \tag{42}$$

The exit boundary conditions were specified as traction free with the specification of  $t_x = 0$  and  $t_y = 0$ .

Mesh schematic and contours of the u-velocity component, v-velocity component, and pressure are exhibited by Figure 1 for a Reynolds number of 20. Figure 2 shows the  $L^1$  error for the u component and v component of the velocity. On a semi-log plot, we obtain a straight line with increasing  $p_{level}$  and the error norm. We also obtain spectral convergence of the  $L^2$  error. This has been demonstrated in Figure 3. The above example demonstrates the spectral/hp element framework developed for solving problems presented in the following examples. Spectral convergence of the errors was obtained with increasing the polynomial expansion in a generic [2,4] macro mesh with two elements along the X direction and four elements along the Y direction.

Estimates of the time to solve the problem are depicted in Table 1 in seconds. The problem was solved on eight CPU cores.

Table 1. Time to solution.

$p_{level}$	$N_{dof}$	Time (s)
3	91	7
4	153	25
5	231	86
6	325	86 248
7	435	808

Fluids **2024**, 9, 18 12 of 29

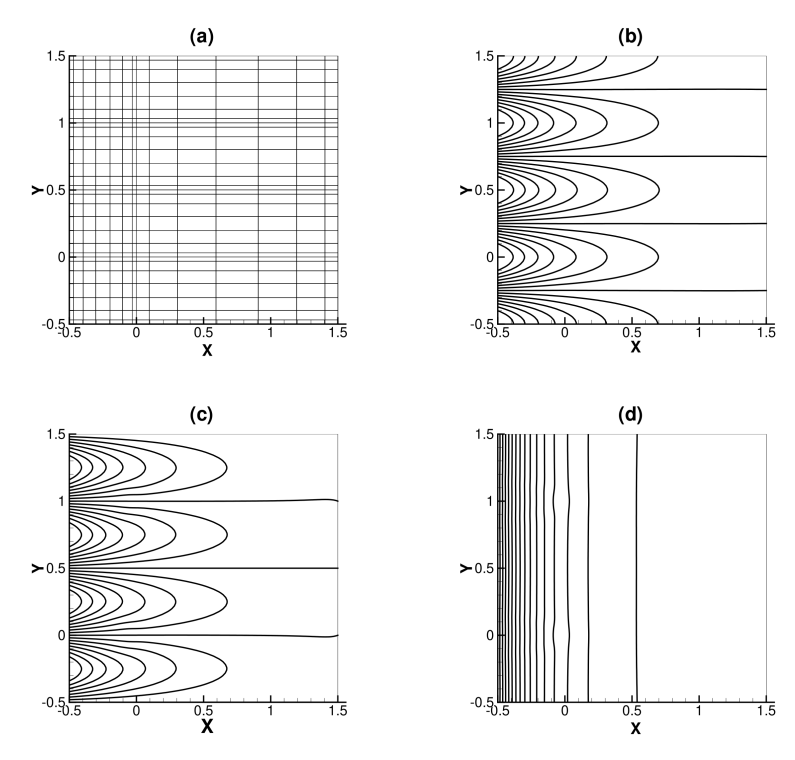


**Figure 1.** Mesh and contour plots of Kovasznay flow: (a) mesh, (b) u component, (c) v component, and (d) pressure.

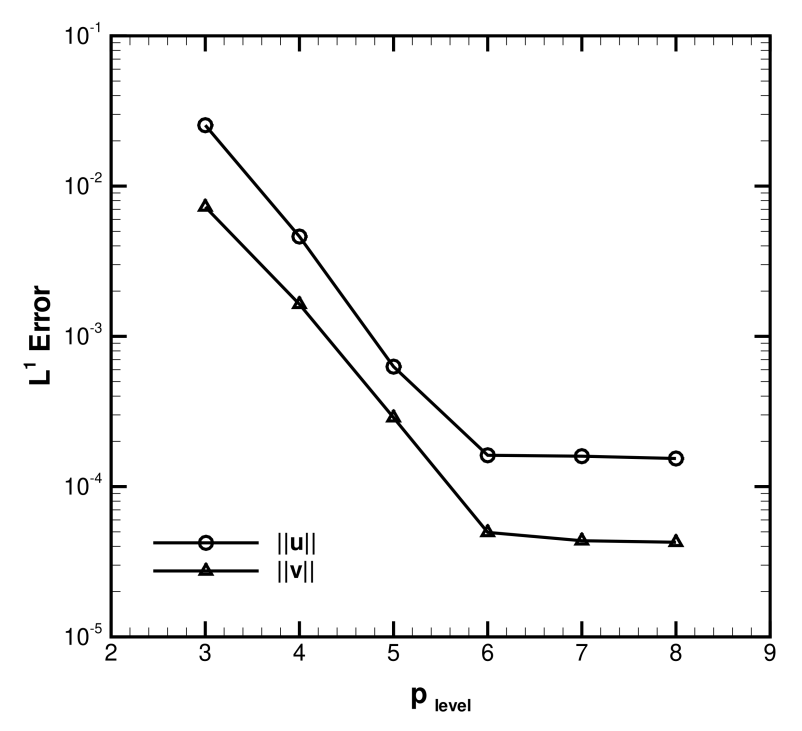


**Figure 2.**  $L^1$  convergence plots of Kovasznay flow.

Fluids **2024**, 9, 18

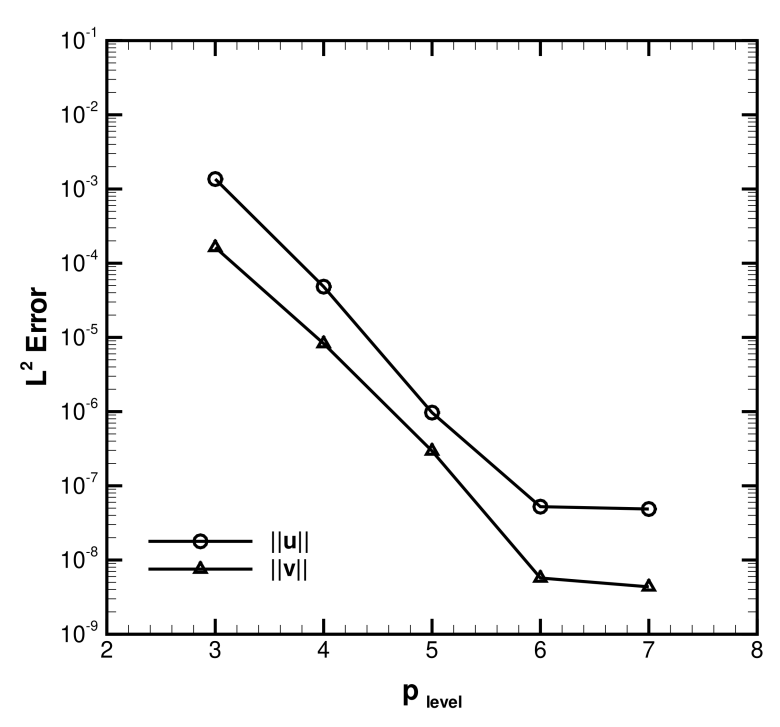


**Figure 3.**  $L^2$  convergence plots of Kovasznay flow.

#### 5.2. Sod's Shock Problem

Sod's shock problem represents a classical problem of compressible flow computations for evaluating the accuracy of a numerical scheme, since there is an analytical solution available. The problem involves a differentially pressurized chamber with a high-density and high-pressure region and a lower-density and low-pressure region separated initially by a diaphragm. At the time instant, t=0, the diaphragm is allowed to break, and the problem evolves in space–time. The driving force for this problem is the initial separation of the high density and high pressure region that interacts with the low-pressure side. Shock propagation along the X axis is the problem we wish to examine.

We consider the computational domain of size  $1 \times 0.1$  discretized into  $20 \times 4$  elements with a polynomial expansion of 4 ( $p_{level} = 4$ ) in each element of the macro mesh. The total number of nodes in the problem was 1377 with a total of 5508 degrees of freedom. The initial condition of the shock tube is specified as:

$$(\rho, u_1, u_2, p) = (1, 0, 0, 1) \text{ for } x \le 0.50$$
  
 $(\rho, u_1, u_2, p) = (0.125, 0, 0, 0.1) \text{ for } x \ge 0.50$  (43)

The problem involved setting up the initial conditions as prescribed and the appropriate boundary conditions for the problem. The top and bottom faces of the domain were considered to have no penetration and free slip boundary conditions ( $\rho u = freeslip$  and  $\rho v = 0$ ). The left and right faces of the domain were not specified to have any boundary conditions. These boundaries are allowed to be traction free with  $t_x = 0$  and  $t_y = 0$ . The initial Mach number for the domain was specified to be a low value of 0.01. The initial velocity profile of the whole domain was considered to be a state of quiescence ( $\rho u = 0$  and  $\rho v = 0$ ). The problem was simulated as a transient with an end time of 0.2 with a time step of 0.001. It is important to note that we did not allow the solution features (shock, expansion fan, and contact discontinuity) to reach the boundaries during the problem evolution. Figure 4 exhibits the spectral/hp mesh for a section of the domain that was used for solving the Sod's shock problem. A contour plot of the conservative variable  $\rho$  at a time of t = 0.2 has been included in the figure. Both definitions of the shock-capturing parameters Equations (22) and (25) were tested for the Sod's shock tube. Figure 5 (left) shows the final density profile at the horizontal mid-plane of the shock tube compared

Fluids **2024**, 9, 18 14 of 29

with the semi-analytical solution and both definitions of the shock capturing parameters. As can be observed, there are good agreement between the semi-analytical solutions and the predicted solutions obtained from the stabilized spectral solver. A comparison of the  $u_1$ -velocity is depicted in Figure 5 (right) across the horizontal mid-section of the domain. We observe a slight oscillation in the velocity for both based stabilization parameter definitions. From the agreement for this problem we realize a fairly coarse discretization of  $20 \times 4$  elements provides good agreement with the solutions available for both shock capturing parameters. The  $YZ\beta$  stabilization parameter was tested with an averaging of the parameter with values of  $\beta = 1$  and  $\beta = 2$  per Equation (28).

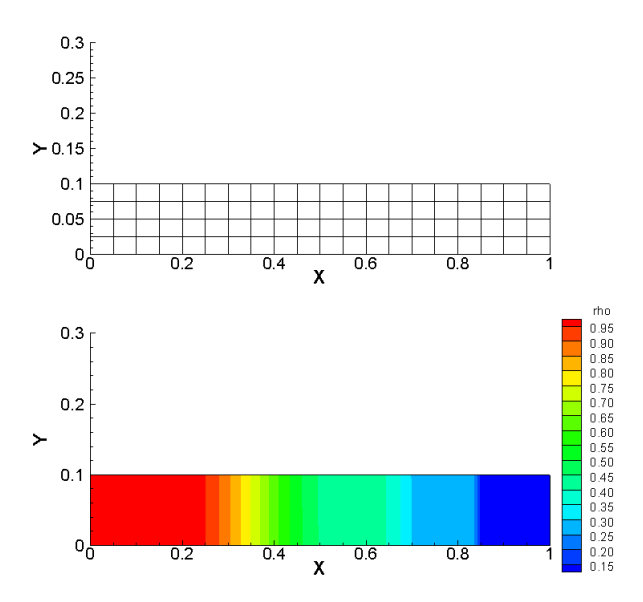


**Figure 4.** Sod's shock problem—Mesh and contour plot of  $\rho$ .

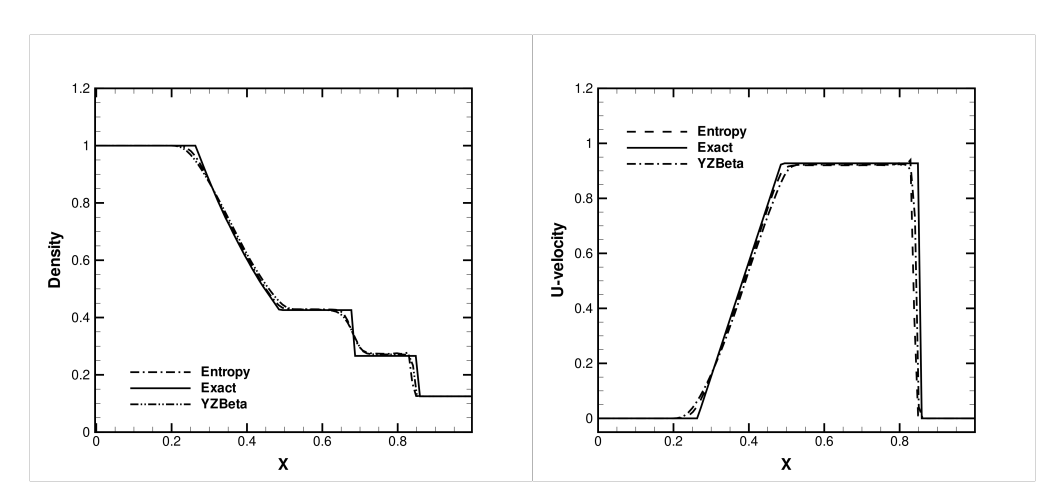


Figure 5. Sod's shock problem final profiles: density (left) and x-velocity (right).

## 5.3. Oblique Shock

The problem involves the solution of a two-dimensional flow entering a flat domain at an angle of  $-10^{\circ}$  with respect to the horizontal plane. The inflow Mach number is 2.0, over a flat plate. The reason for the formation of the shock in this problem is the incoming high speed flow inclined at a predetermined angle, which results in the formation of a shock wave from the bottom of the incident flat plate. This flow results in a shock that emanates at an angle of  $29.3^{\circ}$  from the leading edge of the plate. Analytic solutions exist for the

Fluids **2024**, 9, 18 15 of 29

post-shock region based on the Rankine–Hugoniot relations, and the following describes the inflow and the jump conditions in the post-shock region:

Inflow 
$$\begin{cases} M = 2.0 \\ \rho = 1.0 \\ u_1 = cos10^{\circ} \\ u_2 = -sin10^{\circ} \\ p = 0.17857 \end{cases}$$
 Outflow 
$$\begin{cases} M = 1.64052 \\ \rho = 1.45843 \\ u_1 = 0.88731 \\ u_2 = 0.0, \ p = 0.30475 \end{cases}$$
 (44)

The computational domain is of size  $1 \times 1$ , which is discretized into a macro mesh of  $10 \times 10$  elements. A polynomial expansion of 4 was considered in each element of the macro mesh. The problem involved the solution of 26,244 degrees of freedom with a total number of nodes of 6561. All four free stream Dirichlet boundary conditions were specified on the top and the left boundaries of the computational domain. The bottom surface of the domain was considered to have free slip (for the *u*-component of the velocity). The u-component of the domain was considered to have no penetration boundary condition on the bottom face. No boundary condition was specified on the right face. Figure 6 shows the setup of the problem domain along with inflow and outflow flow profiles. The end time of the transient was determined as 3.0 with a time step of  $\Delta t = 0.01$ . We utilize both definitions of the shock-capturing parameters as given by Equations (22) and (28) for the Oblique shock problem. Figure 7 (left) illustrates the development of the density profile at the vertical slice location set at x = 0.9 at the attainment of steady-state for both shock capturing parameters. The results show the shock profile predicted by the spectral/hp element method versus the exact solution for this problem. It is observed from the figure that the spectral/hp element approximation provides an accurate resolution of the shock location as compared to the exact solution to the problem. The density profiles were also found to be in agreement with SUPG and multiscale stabilized solutions are presented in Bento et al. [52]. A slight deviation in the density at the Y = 0 was due to slight variation during a long time integration of the partial differential equation. Appropriate care to mesh refinement and *hp* adaptation can address the slight discrepancy observed.

Figure 7 (right) compares the pressure profile at the vertical cross section at the x-coordinate location of x=0.9. For both shock-capturing parameters, the results are in good agreement with the exact solution to this problem. The entropy-based definition of the shock parameter provided a slightly sharper resolution of the shock; however, in later experiments, it was realized that  $YZ\beta$  parameter performed better.

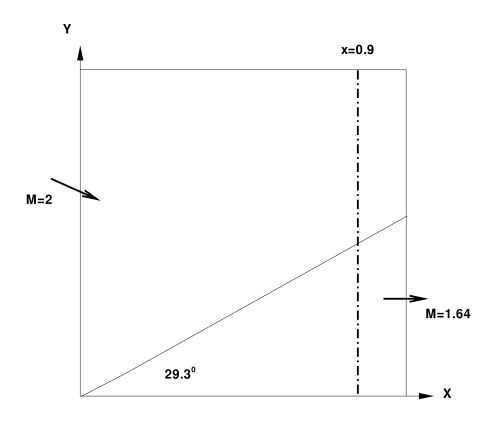
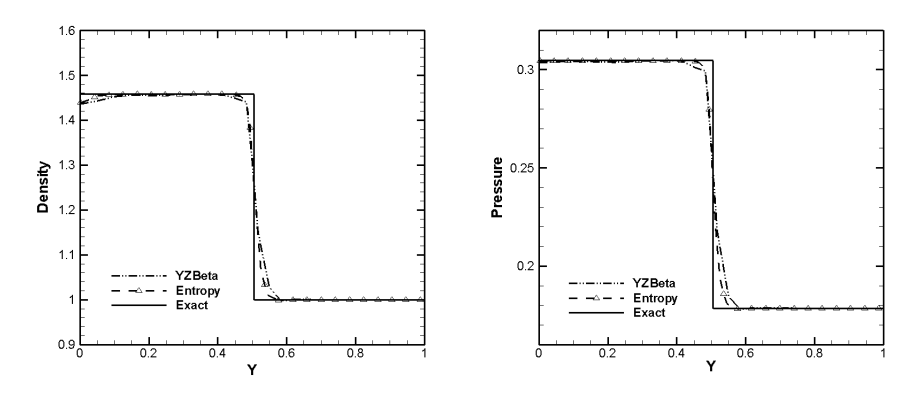


Figure 6. Oblique shock problem description.

Fluids **2024**, 9, 18



**Figure 7.** Oblique shock problem—Profiles at x = 0.9.

#### 5.4. Reflected Shock Problem

We consider the problem of shock reflection from the bottom wall. In this problem, we have an incoming flow aligned with the x axis interacting with another flow which impinges on a flat plate that is aligned at an angle of  $29^{\circ}$ . A shock reflection happens due to this shock—shock interaction problem from the bottom of the plate. This classical solution has ramifications in the design of shock boundary layer interaction (SBLI) of ramjets. The initial shock train formation recovers the formation of a classical 'step profile', which we recover as the solution to this problem. The flow has three regions with nomenclature M1, M2, and M3. The computational domain is separated into different domains with two shocks separating them.

Figure 8 depicts the computational domain and the problem configuration with delineation of the different regions of shock discontinuity. The steady-state solution of the problem is provided as follows:

$$M1 \begin{cases}
M = 2.9 \\
\rho = 1.0 \\
u_1 = 2.9 \\
u_2 = 0.0 \\
p = 0.714286
\end{cases}
M2 \begin{cases}
M = 2.3781 \\
\rho = 1.7 \\
u_1 = 2.61934 \\
u_2 = -0.50632 \\
p = 1.52819
\end{cases}
M3 \begin{cases}
M = 1.94235 \\
\rho = 2.68728 \\
u_1 = 2.40140 \\
u_2 = 0.0 \\
p = 2.93407
\end{cases}$$
(45)

We consider the domain of length  $[0,4.1] \times [0,1]$ . All the four boundary conditions are specified on the left and the top boundaries. Obtaining a steady state for this problem is of interest. At the bottom boundary, we specify the free slip and no penetration boundary conditions. No boundary conditions are specified at the outflow boundary. The flow is initialized with the flow conditions in region M1. For the  $YZ\beta$  parameter (based on Equation (28)), the initialization of the reference values was done with the values in region M2 as  $U_r = (\rho_{M2}, \rho u_{1M2}, \rho u_{2M2}, \rho e_{M2})^T$ . The entropy-based shock parameter had issues with convergence till the end time for this problem. Even reducing the time step did not seem to provide a converged solution and the program terminated prematurely. We discretize the domain into a macro mesh of  $40 \times 10$  elements with a polynomial order of 4 in each element. The problem had 6601 nodes in the problem with a total number of degrees of freedom of 26,404. The problem was discretized into a uniform mesh without regard to finer mesh density near the predetermined shock locations. This provides flexibility in the solution and also tests the robustness of the solver for generic problems. An alternative is the use of an adaptive hp refinement; however, as an exercise, we test the robustness of the solver. We utilize a time step of 0.000125 with an end time of 3.0 units. Figure 9 (left) provides the density profile along the horizontal line located at y = 0.25 for the problem considering the  $YZ\beta$  shock capturing definition and the exact solution for this problem. Fluids **2024**, 9, 18 17 of 29

The jumps in the density locations are in agreement with the results presented by Bento et al. [52] and Senga [50]. A reduction of the  $L^2$  density residual with nondimensional time is presented in Figure 9 (right). As can be observed from the figure, there is a gradual reduction of the residual with time till the end time of 3.0. There is a three-order-of-magnitude reduction in the residual over a time interval of 3.0, which is similar to what was found by Catabriga and Coutinho [37]. The entropy-based definition of the stabilization parameter was not found to attain convergence for this problem for the full-time integration, whereas the  $YZ\beta$  parameter was found to have better convergence for this numerical experiment.

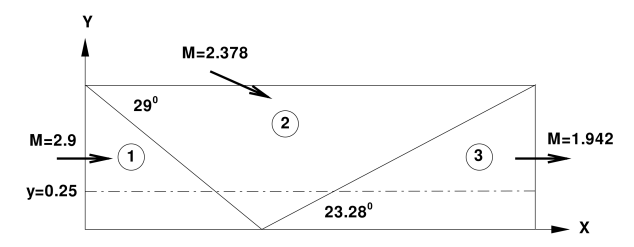


Figure 8. Reflected shock problem description.

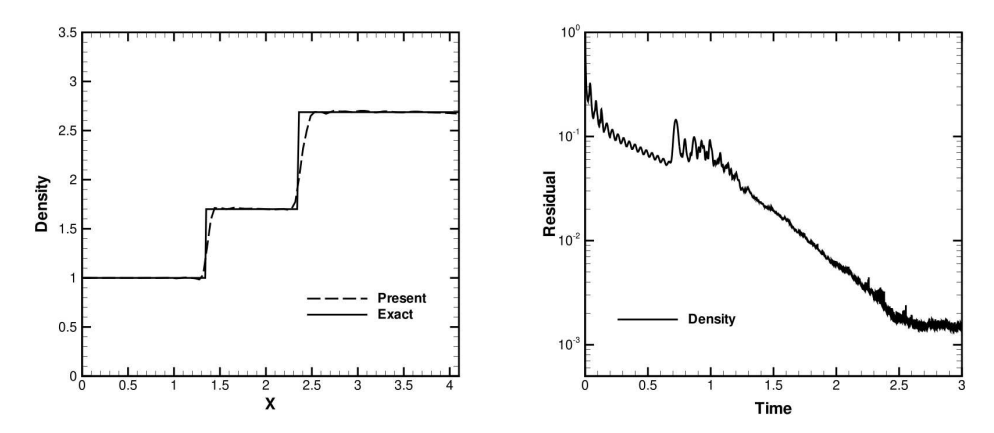


Figure 9. Reflected shock problem—density solutions.

# 5.5. 2D Explosion Problem

We consider the space–time evolution of a blast wave in two dimensions specified in Bento et al. [51]. The problem domain is of size  $2 \times 2$ . There exists a high-density and high-pressure region in the shape of an initial circle centered at (1,1). The radius of the circle is 0.40, and it is allowed to evolve in space–time. The formation of a shock expansion happens since this problem replicates a blast wave solution in two dimensions. This explosion is because of the high density high pressure region that is expanding in time. Figure 10 presents the domain size and the circular-shaped region of high density and pressure centered at (1,1). The initial density and pressure in the domain and the circular-shaped region is specified as follows:

$$(\rho, u_1, u_2, p) = (1, 0, 0, 1) \text{ for } r \le 0.40$$
  
 $(\rho, u_1, u_2, p) = (0.125, 0, 0, 0.1) \text{ for } r \ge 0.40$  (46)

where r denotes the radial coordinates from the centroid of the square. No boundary conditions were specified on all the boundaries of the domain. This specification amounts to specification of traction-free boundaries on all sides of the computational domain. Furthermore, the problem was not simulated for a long enough time for the waves to reach the boundaries of the computational domain.

Fluids **2024**, 9, 18 18 of 29

The problem was discretized with a macro mesh of  $40 \times 40$  element with a polynomial order of 4 in each element. This resulted in  $161 \times 161$  nodes in the problem. The total number of variables solved in the problem was, thus, 103,684.

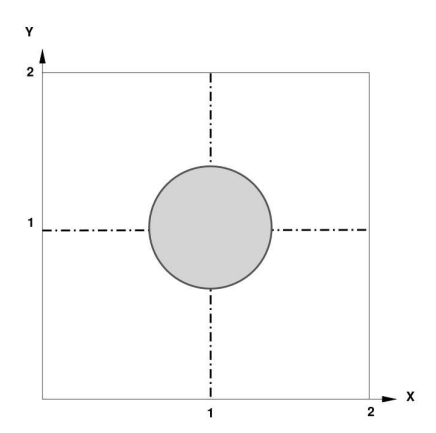


Figure 10. Two-dimensional explosion problem description.

Figure 11 (left) shows the final contour plot of the density over the domain at a time instant of t=0.25 considering the  $YZ\beta$  shock capturing parameter from Equation (28). Once again, the solution with the entropy-based shock parameter does not perform well. The problem was solved as a transient with a time increment of 0.000125. The radial variation of the density for the problem at the time instant of t=0.25 has been presented in Figure 11 (right). The figure compares the results obtained with the semi-analytical solution provided by Toro [54] as the reference solution. The numerical results are in reasonably good agreement for this problem with the reference solution. With an increase in the  $p_{level}$  from 4 to 5, there is lesser diffusion attributed to a more accurate solution to the transient Euler equation.

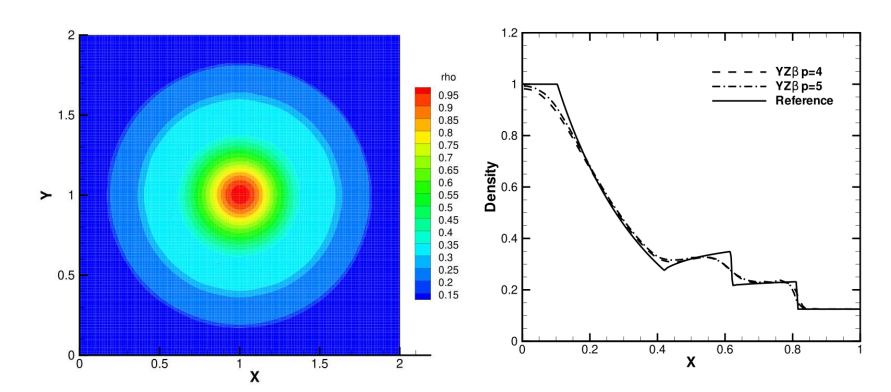
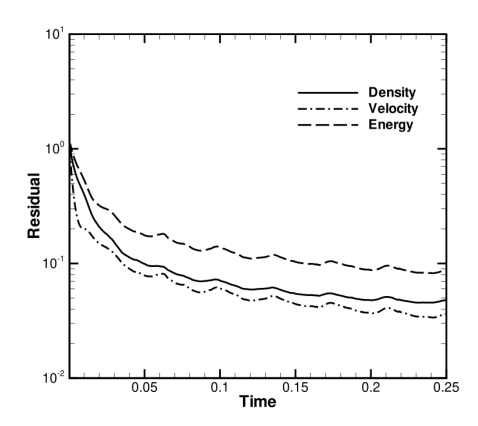


Figure 11. Two-dimensional explosion problem—density solutions.

The  $L_2$  errors of the  $\rho$ ,  $\rho u_1$ , and  $\rho e$  have been depicted in Figure 12 for the solution considering the  $YZ\beta$  parameter. It is observed a time reduction of  $L_2$  residuals within one and a half order of magnitude. Experience with other codes (Air Force Research Laboratory codes Aerothermodynamic Nonequilibrium Detailed Energy Exchange—ANDEE) also provides an explanation for the slow residual reduction. Scaling of the residual with time is often employed rather than direct  $L^2$  residual evaluation. This, coupled with localized time stepping, can provide a slightly better reduction of the residuals [5].

Fluids **2024**, 9, 18



**Figure 12.** Two-dimensional explosion problem— $L_2$  residual.

## 5.6. 2D Inviscid Flow Past Step Problem

We consider flow past a two-dimensional step of height a at Mach number 3.0. In this problem, there is an incoming flow aligned with the x-axis that interacts with an obstruction. The shape of the obstruction is a step with a sharp corner. The formation of a standing shock is because of this flow that is restrained by the step and forms a bow shock. This is a challenging problem since there is a bow shock formation in front of the step and the near over-expansion of the flow behind the step. A sharp corner ahead of the step also poses a problem for high-order methods, and exponential convergence of the spectral element method at the corner of the step can be an issue. Possible pollution of the solution may start at the singularity of the step and not adequate stabilization of the method across the domain. This can lead to significant obstacles in obtaining a solution with instability and convergence issues of the formulation. We address the solution of the above problem with Overflow and the present definitions of stabilization parameter with spectral hp element methods.

## 5.6.1. Spectral/*hp* Framework

The computational domain is considered a bottom subdomain of length  $2 \times 0.5$  and a top section of dimensions  $4 \times 3.5$ . Thus, the step height was taken as a = 0.5. The computational domain along with the approximate location of the stagnation line, AB, is exhibited in Figure 13.

The inlet to the computational domain was considered to have all inflow conditions specified as  $(\rho, \rho u_1, \rho u_2, \rho e) = (1.0, 1.0, 0.0, 0.6984)$ . The reference values of the inflow parameters  $U_r$  were specified as  $U_r = (1.0, 1.0, 1.0, 0.6984)^T$  in the determination of the  $YZ\beta$  parameters in Equation (28). Each face of the computational domain other than the inlet face was specified to have a slip boundary condition, and the orthogonal component of the velocity was specified to be zero. We consider an inflow Mach number of 3.0. Only the solution considering  $YZ\beta$  shock-capturing parameter is executed.

The computational domain was discretized into a macro mesh of  $20 \times 10$  and  $40 \times 20$  elements for the bottom and top subdomains, respectively. A constant polynomial expansion ( $p_{level}$ ) of 5 and 6 were considered in each element of the spectral discretization of the domain. The problem was discretized into 19,481 nodes with a total number of variables of 77,924 that comprised the discretization of the computational domain for the case with  $p_{level}$  of five in each element. The simulation was started with a constant time step of 0.001 for both p levels. The end time of the simulation was taken as 3.0.

Fluids **2024**, 9, 18 20 of 29

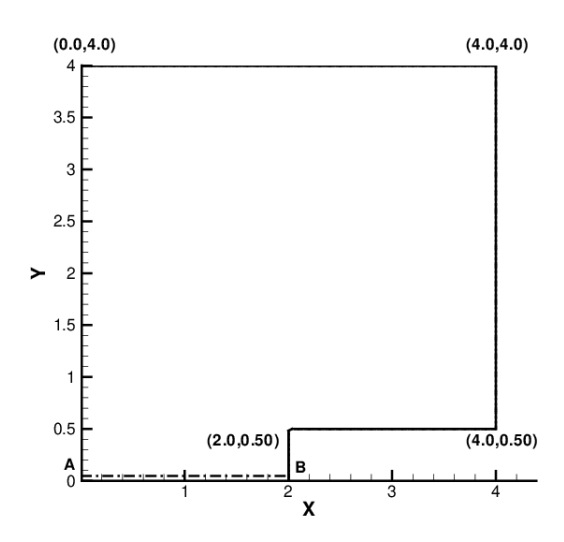
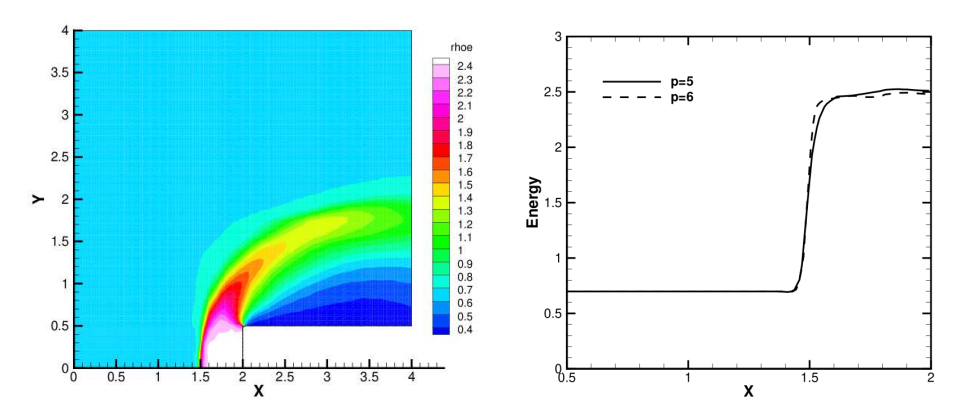


Figure 13. Two-dimensional flow past step problem—domain description.

Figure 14 (left) shows the development of the contour plot of the total energy in the computational domain. A plot of the total energy along the stagnation line AB in Figure 13 has been provided in Figure 14 (right). From the plot, the location of the shock wave is found to be approximately at 1.5. A higher  $p_{level}$  of 6 was found to provide a sharper shock resolution in the figure.



**Figure 14.** Two-dimensional flow past step problem—total energy solutions with the  $YZ\beta$  shock-capturing parameter.

## 5.6.2. OverFlow Problem

The problem was solved separately with the NASA code OverFlow [10]. The domain of discretization was taken as a computational domain of length [10,10]. The size of the obstruction was considered of length [1,1]. The whole domain was discretized into [160  $\times$  160] quadrilateral elements. A fifth-order weighted, essentially nonoscillatory scheme (WENO-5) was considered for analysis. A high-order implementation for Overflow provides a comparison of the high-order framework with a high-order finite volume formulation. A van Albada flux limiter was used in conjunction with the WENO scheme. The problem was solved for an end time of 3.0 with time increments of 0.001. The obstruction was considered delineated with the fictitious domain method (FDM) with a specified density inside the obstruction.

The plot of the  $u_1$  component of the velocity along the stagnation line is depicted in Figure 15. From this figure, the location of the shock discontinuity is at the x location of 1.5. A higher  $p_{level}$  provides a slight improvement in delineating the shock location. The figure also provides a p convergence of the results between different polynomial expansions for the new stabilization parameter. From OverFlow code results, we obtain the shock standoff

Fluids **2024**, 9, 18 21 of 29

distance of a = 0.5. The new definitions of the stabilization parameters reproduce an accurate shock profile.

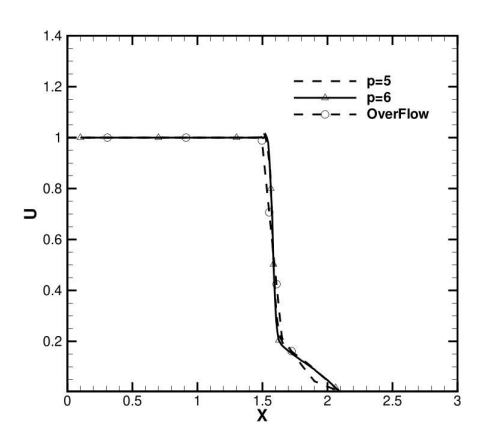


**Figure 15.** Two-dimensional flow past step problem— $u_1$ -velocity solutions.

## 5.7. Implosion Problem

We consider the 2D implosion problem for analysis. The problem entails the solution of the Euler equation in two dimensions. A two-dimensional domain of length [0.6, 0.6] units has a square of half diagonal length 0.15 units with the center located at [0.3, 0.3]. A low-density, low-pressure domain exists inside the square with the exterior of the square, being the high-density outer region. An implosion occurs because of this density and pressure difference. The outer high-pressure region exists, which pushes into the low density and low pressure region, and because of this density and pressure difference, a shock implosion problem results. The equation of the line that separates the two regions are as follows:

$$y + x = (x_c + y_c \pm a) \tag{47}$$

and

$$y - x = (-x_c + y_c \pm a) \tag{48}$$

where  $(x_c, y_c)$  denote the center of the square. In the present case, we use the center coordinates of (0.30, 0.30). The half-diagonal length of the domain was taken as a = 0.15.

The low-pressure region inside of the square domain has an initial density of 0.125 and an initial pressure of 0.14. The outer high pressure and density of the domain are given as 1.0 and 1.0, respectively. The computational domain is shown in Figure 16. The domain was discretized into  $80 \times 80$  spectral elements. A Legendre expansion of order 6 was used in the domain to resolve the problem. At time t=0, the walls of the low-pressure square region break, and the problem is allowed to evolve in space–time. The time increment for stepping the problem was taken as 0.00125. Reflecting boundary conditions were specified on the outer walls of the domain, which entail enforcing the normal component of the velocity to zero. Free slip is allowed on the  $\rho u_1$  component. Figure 17 depicts the density plot for compressible flow computations at times of t=0, t=0.04338, t=0.062, and t=0.075125, respectively.

The implosion of the low-density region with the high-pressure region is evident in Figure 17. We utilized the  $YZ\beta$  (Equation (28)) parameter since this definition was found to be more robust in the context of spectral computations. The results are in agreement with the results presented in Nazarov [55].

Fluids **2024**, 9, 18 22 of 29

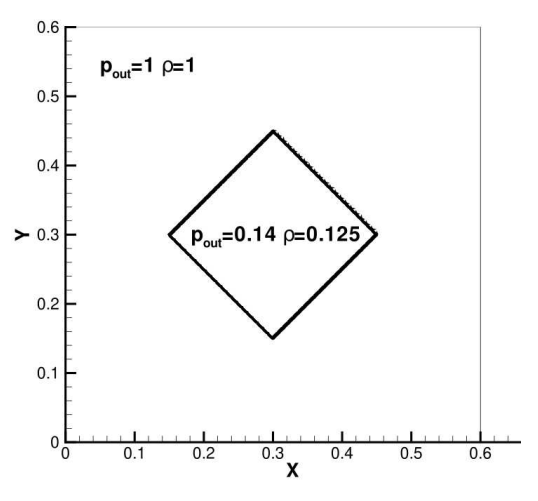
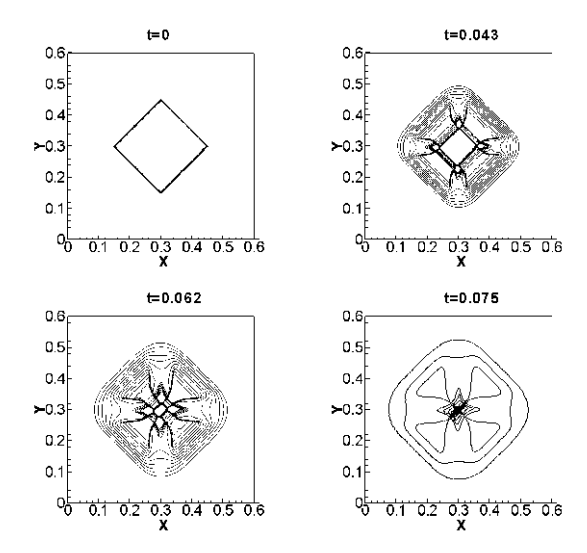


Figure 16. Two-dimensional implosion problem—domain description.



**Figure 17.** Two-dimensional implosion problem—density contours.

# 5.8. AS-202 Capsule

We examine problems involving atmospheric reentry at high Mach numbers. The geometry in consideration is the AS-202 capsule. Initial designs of hypersonic flow fields around reentry vehicles can be described with Modified Newtonian methods. More detailed designs require a complete CFD computation. Considerations of nonequilibrium effects in high-speed flow computations are relevant in the hypersonic regime. Departure from thermal equilibrium has to be accounted for in high-speed flow applications. In the present development, we do not consider nonequilibrium effects and neglect vibrational and electronic states of energy transfer for molecules. During the development of the Apollo program for lunar landing, various flight experiments were conducted by NASA to quantify aerothermal characteristics around the reentering command module [56]. A reentry capsule consists of a blunt forebody, followed by a conical afterbody with a straight or rounded base. Once the Apollo entry vehicle design was determined, two flight tests of the actual command module (AS-201 and AS-202) were conducted at super orbital entry velocities resulting from suborbital boosted trajectories with an intentional skip maneuver. The problem entails examining the shock in front of a reentry capsule, which obstructs the flow at a certain angle of attack. Because of the presence of an obstruction, we have the formation of a standing shock in front of the capsule. Examining the flow around such a reentry vehicle has implications in hyper velocity flow applications and a better understanding of the shock physics when further studies examine nonequilibrium effects. A high-order Fluids **2024**, 9, 18 23 of 29

implementation also examines the possiblity of recovery of a higher pitching moment than that has been reported by low-order based CFD studies in the literature for this problem.

Hypersonic flows exhibit complex multi-physics phenomena and very high-temperature increases across the shock. This temperature increase can be described by Rankine–Hugoniot conditions or the normal shock relations as the first estimates. We consider atmospheric reentry at Mach number 5.0 and 7.0. Let us consider an inviscid solution for the external flow analysis of the AS 202 capsule. The capsule was considered to have the normal component of the velocity prescribed to zero. Figure 18 presents the outer mold line for the AS-202 capsule. The problem was discretized into both coarse and fine meshes. The coarse mesh consisted of a macro mesh with a total of 4920 elements with a total of 79,378 nodes in the problem. A finer mesh considered a total of 8000 elements and a total of 128,802 nodes. Both meshes considered a polynomial expansion of 4 in each element. The problem specification required prescribing the inflow velocity at the inlet and the top and bottom of the computational mesh, as shown in Figure 19.

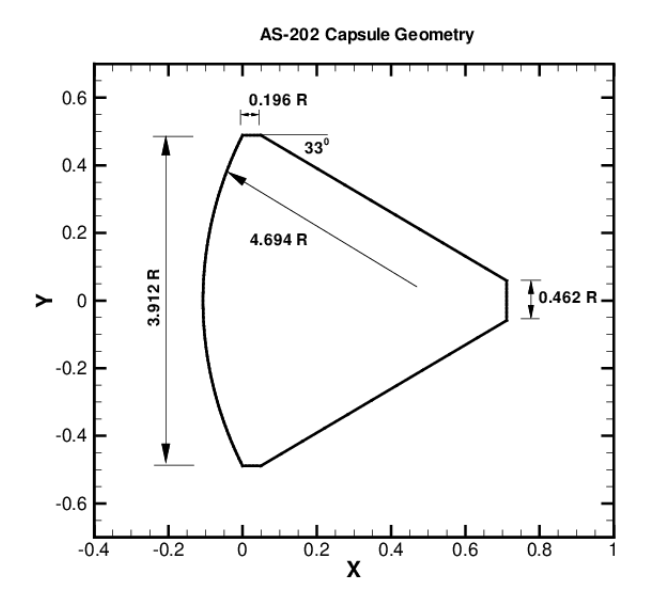


Figure 18. AS-202 capsule geometry.

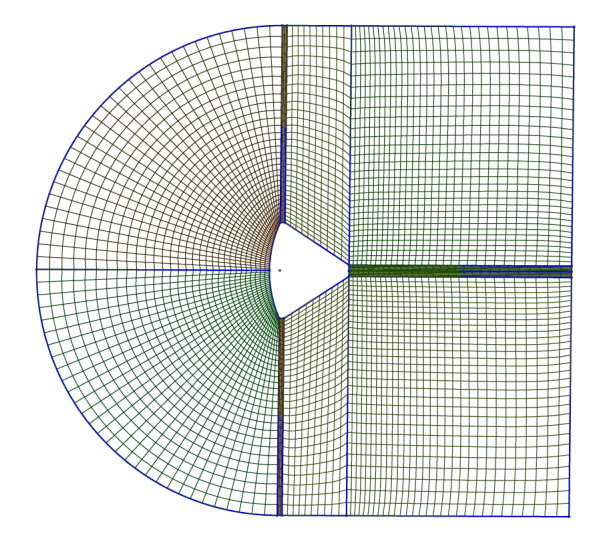


Figure 19. Mesh for AS-202 capsule.

We consider as a validation exercise the external flow field around the capsule at Mach 7.0. A contour plot of the  $\rho v$  component of the velocity is presented in Figure 20 on

Z\_X

Fluids **2024**, 9, 18 24 of 29

the finer mesh. A comparison of the density has been presented in Figure 21 for both fine and coarse meshes along the stagnation line.

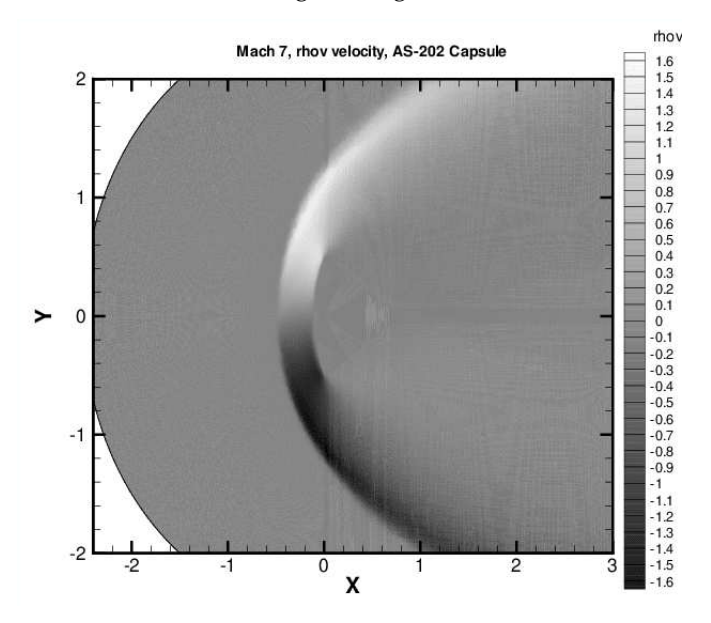


**Figure 20.**  $\rho v$  component of velocity Mach 7.0.

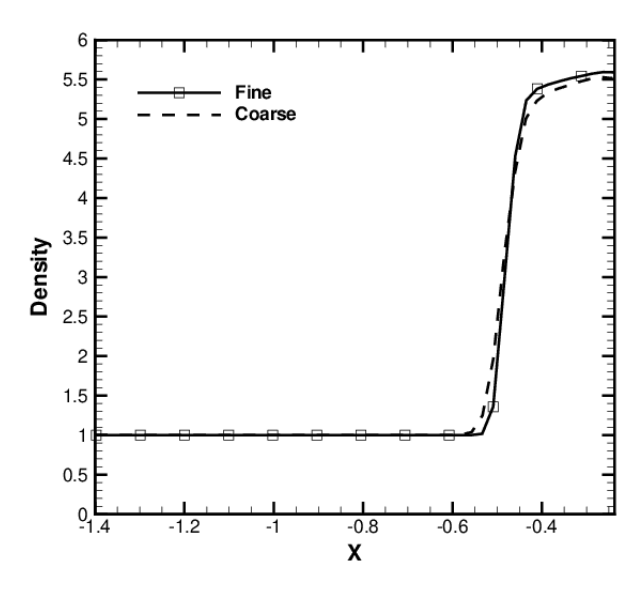


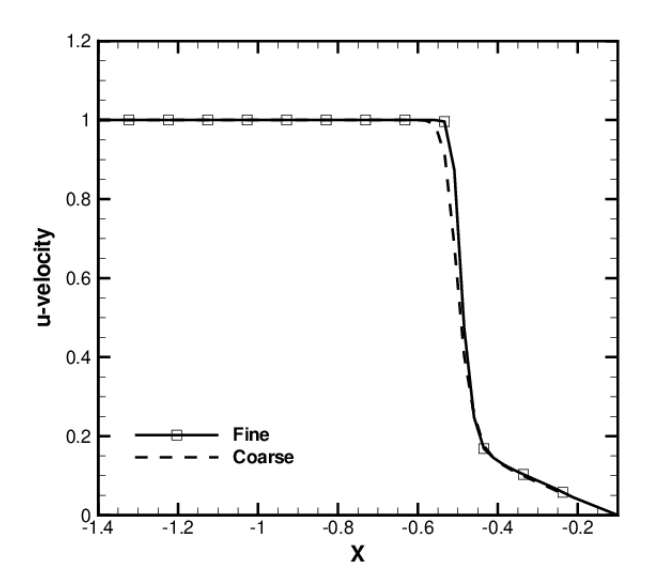
Figure 21. Density across shock along stagnation line Mach 7.0.

Figure 22 presents the u component of the velocity for the velocity profile along the stagnation line. There is excellent agreement between the density and the velocity profiles along the stagnation line between the coarse and fine meshes providing a numerical validation process. We utilized the  $YZ\beta$  parameter for analysis of the problem considered. After the above validation exercise, we examine the whole flight envelope for the AS-202 capsule on the finer mesh.

In order to provide an exhaustive application, a part of the flight envelope was considered with different angles of attack varying from 3 through 18 degrees for a Mach number of 5.0. We provide a parametric study of the coefficients lift and lift over drag (L/D) ratio. The range of angles of attack considered were (3,6,9,12,15,18) with flight conditions of Mach 5.0. The flow was allowed to reach a steady state with an end time of 15.0 with a time increment of 0.005. This study was chosen to provide an application involving external aerodynamics for a very complicated atmospheric reentry problem. The problem was benchmarked with a separate code  $CREATE^{TM}$ -AV Kestrel fluid solver,

Fluids **2024**, 9, 18 25 of 29

kCFD. Figure 23 presents the lift coefficient for AS-202 capsule at varying angles of attack compared with kCFD. A comparison between Lift over Drag L/D ratios between the present results and kCFD has been provided in Figure 24. Figure 25 shows a contour plot of the Mach number for the capsule at angle of attack of  $18^{\circ}$ . Figure 26 depicts contour plot of  $\rho v$  component of velocity for the capsule. We observe revised definitions of stabilization parameters provide excellent agreement in predictions of lift and drag coefficients through the flight envelope.



**Figure 22.** *u*-velocity across shock along stagnation line Mach 7.0.

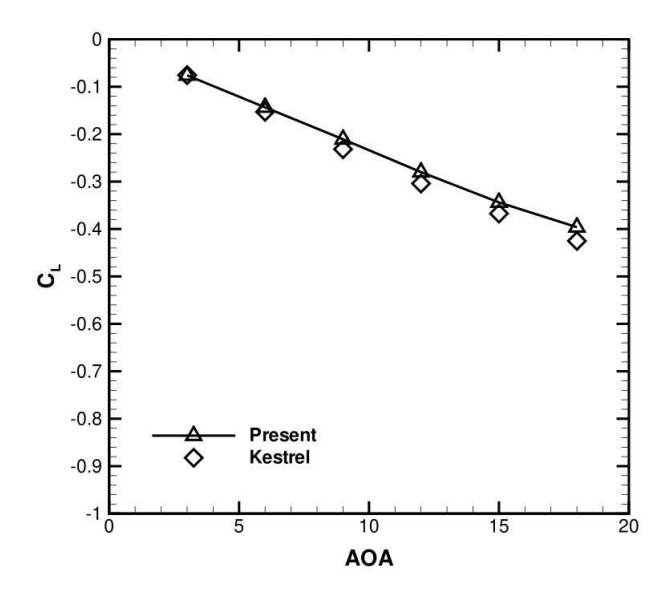
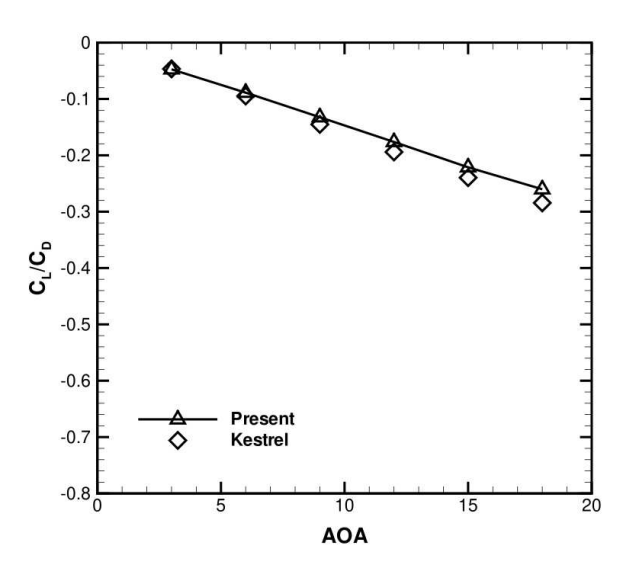


**Figure 23.** Lift coefficient for AS-202 capsule Mach 5.0.

Fluids **2024**, 9, 18 26 of 29



 $\textbf{Figure 24.} \ Lift/drag \ coefficient for \ AS-202 \ capsule \ Mach \ 5.0.$ 

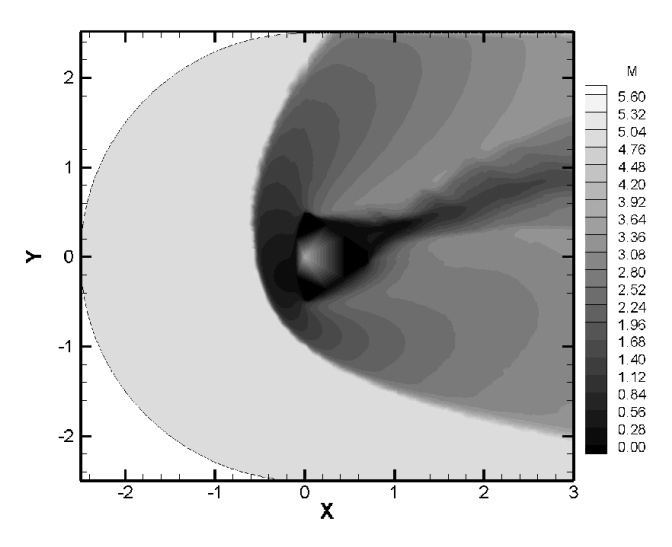


**Figure 25.** Contour plot Mach number 5.0 and AOA  $18^{\circ}$ .

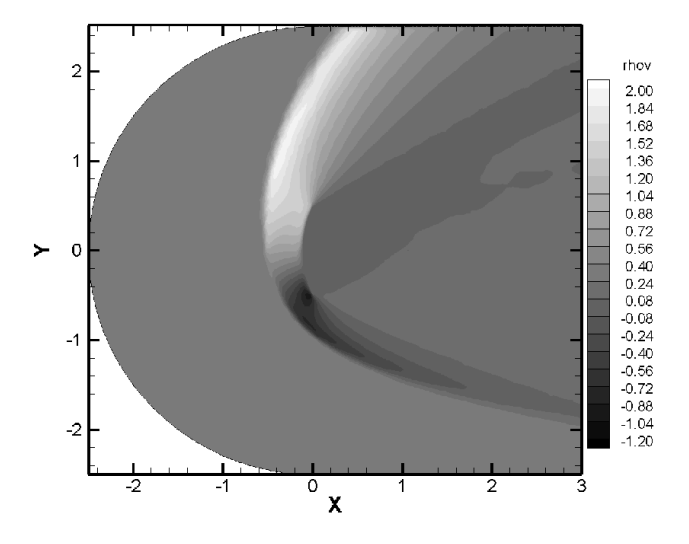


**Figure 26.** Contour plot  $\rho v$  component Mach 5.0 and AOA 18°.

Fluids **2024**, 9, 18 27 of 29

#### 6. Conclusions

High-order spectral /hp element methods were introduced and applied for computations involving compressible flow problems without viscous contributions within the stabilized finite element framework. A series of benchmark problems involving the solution of Euler equations were addressed, and concrete applications were provided. Solutions were compared for the whole flight envelope, and excellent agreement was found with other CFD solvers. The high-order formulation was found to provide results that are in agreement with benchmark results in the literature. Consideration of aerothermodynamic effects with appropriate compartmentalization of energy states of various diatomic species in the hypersonic regime is the subject matter of current research activities.

#### 7. Dedication

This paper is dedicated to the memory of Dr. N. Prasad and Dr. Y. Feng.

**Author Contributions:** Conceptualization, R.R.; methodology, R.R. and L.C.; software, R.R.; validation, R.R.; formal analysis, R.R.; investigation, R.R. and L.C.; resources, G.A.; data curation, G.A.; writing—original draft preparation, R.R. and G.A.; writing—review and editing, R.R. and G.A.; visualization, R.R.; supervision, L.C. and R.R.; project administration, L.C. and G.A.; funding acquisition, G.A. All authors have read and agreed to the published version of the manuscript.

**Funding:** G.A. acknowledges financial support from the National Science Foundation under grant #2314303 and by the Air Force Research Laboratory under agreement number #FA9550-23-1-0241.

Data Availability Statement: Data are contained within the article.

**Acknowledgments:** The reviewers are greatly acknowledged for their comments, which made us improve the quality of the present article.

Conflicts of Interest: The authors declare no conflicts of interest.

#### References

- 1. Hughes, T.J.; Tezduyar, T.E. Development of Time-Accurate Finite Element Techniques for First Order Hyperbolic Systems with Emphasis on the Compressible Euler Equations; NASA: Washington, DC, USA, 1982.
- 2. Hughes, T.J.; Tezduyar, T.E. Finite element methods for first-order hyperbolic systems with particular emphasis on the compressible Euler equations. *Comput. Methods Appl. Mech. Eng.* **1984**, 45, 217–284. [CrossRef]
- 3. Tezduyar, T.; Hughes, T. Finite element formulations for convection dominated flows with particular emphasis on the compressible Euler equations. In Proceedings of the 21st Aerospace Sciences Meeting, Reno, NV, USA, 10–13 January 1983; p. 125.
- 4. Prabhu, D.K.; Tannehill, J.C. Numerical solution of space shuttle orbiter flowfield including real-gas effects. *J. Spacecr. Rocket.* **1986**, 23, 264–272. [CrossRef]
- 5. Ranjan, R.; Vedula, P.; Vogiatzis, K.; Josyula, E. Numerical Simulation of Hypersonic Turbulent Flows using High Order Methods. In Proceedings of the 2018 AIAA Aerospace Sciences Meeting, Kissimmee, FL, USA, 8–12 January 2018; p. 0980.
- 6. Ranjan, R.; Chronopoulos, A.T.; Feng, Y. Computational algorithms for solving spectral/hp stabilized incompressible flow problems. *J. Math. Res.* **2016**, *8*, 21. [CrossRef]
- 7. Ranjan, R.; Feng, Y.; Chronopolous, A.T. Augmented stabilized and galerkin least squares formulations. *J. Math. Res.* **2016**, *8*, 1. [CrossRef]
- 8. Ranjan, R.; Feng, Y.; Chronopolous, A.T. *Stabilized and Galerkin Least Squares Formulations*; Technical Report; Department of Computer Science, University of Texas at San Antonio: San Antonio, TX, USA, 2016; Volume 1, pp. 1–42.
- 9. Hughes, T.J.; Scovazzi, G.; Tezduyar, T.E. Stabilized methods for compressible flows. J. Sci. Comput. 2010, 43, 343–368. [CrossRef]
- 10. Nichols, R.H.; Buning, P. Users manual for Overflow 2.2. Overflow 2019, v. 2.2n.
- 11. Wissink, A.M.; Sitaraman, J.; Jayaraman, B.; Roget, B.; Lakshminarayan, V.K.; Potsdam, M.A.; Jain, R.; Bauer, A.; Strawn, R. Recent advancements in the Helios rotorcraft simulation code. In Proceedings of the 54th AIAA Aerospace Sciences Meeting, San Diego, CA, USA, 4–8 January 2016; p. 0563.
- 12. Allu, S.; Surana, K.S.; Romkes, A.; Reddy, J.N. Numerical Solutions of BVPs in 2-D Viscous Compressible Flows Using hpk Framework. *Int. J. Comput. Methods Eng. Sci. Mech.* 2009, 10, 158–171. [CrossRef]
- 13. Surana, K.; Ahmadi, A.; Reddy, J. k-version of Finite Element Method for Non-Linear Differential Operators in BVP. *Int. J. Comput. Eng. Sci.* **2004**, *5*, 133–207.
- 14. Ibrahim, M.; Liu, F.; Liu, S. Concentration of mass in the pressureless limit of Euler equations for power law. *Nonlinear Anal. Real World Appl.* **2019**, *47*, 224–235. [CrossRef]

Fluids **2024**, 9, 18 28 of 29

15. Ibrahim, M.; Din, A.; Yusuf, A.; Lv, Y.P.; Jahanshahi, H.; Aly, A.A. Euler equations for isentropic gas dynamics with general pressure law. *Adv. Contin. Discret. Models* **2022**, 2022, 10. [CrossRef]

- Huang, M.; Wang, Y.; Shao, Z. Piston problem for the isentropic Euler equations for a modified Chaplygin gas. *Phys. Fluids* 2023, 35, 016119. [CrossRef]
- 17. Oden, J.T.; Demkowicz, L. hp adaptive finite element methods in computational fluid dynamics. *Comput. Methods Appl. Mech. Eng.* **1991**, *89*, 11–40. [CrossRef]
- 18. Löhner, R.; Morgan, K.; Zienkiewicz, O. An adaptive finite element procedure for compressible high speed flows. *Comput. Methods Appl. Mech. Eng.* 1985, 51, 441–465. [CrossRef]
- 19. Gottlieb, D.; Gottlieb, S. Spectral methods for compressible reactive flows. Comptes Rendus Méc. 2005, 333, 3–16. [CrossRef]
- Cantwell, C.D.; Moxey, D.; Comerford, A.; Bolis, A.; Rocco, G.; Mengaldo, G.; De Grazia, D.; Yakovlev, S.; Lombard, J.E.; Ekelschot, D.; et al. Nektar++: An open-source spectral/hp element framework. Comput. Phys. Commun. 2015, 192, 205–219. [CrossRef]
- 21. Karamanos, G.; Karniadakis, G.E. A spectral vanishing viscosity method for large-eddy simulations. *J. Comput. Phys.* **2000**, 163, 22–50. [CrossRef]
- 22. Cottrell, J.A.; Hughes, T.J.; Bazilevs, Y. *Isogeometric Analysis: Toward Integration of CAD and FEA*; John Wiley & Sons: Chichester, UK, 2009.
- 23. Jaeschke, A.M. Isogeometric Analysis for Compressible Flows with Application in Turbomachinery. Ph.D. Dissertation, TU Delft, Delft, The Netherlands, 2015; pp. 1–107.
- 24. Ranjan, R.; Catabriga, L.; Feng, Y. High-Order Spectral/hp-Based Solver for Compressible Navier–Stokes Equations. *AIAA J.* **2022**, *60*, 2972–2986. [CrossRef]
- 25. Ferziger, J.H.; Peric, M. Computational Methods for Fluid Dynamics; Springer Science & Business Media: Cham, Switzerland, 2012.
- 26. Tannehill, J.C.; Anderson, D.A.; Pletcher, R.H. Computational fluid dynamics and heat transfer. In *Series in Computational and Physical Processes in Mechanics and Thermal Sciences*; CRC Press: Boca Raton, FL, USA, 2016.
- Versteeg, H.K.; Malalasekera, W. An Introduction to Computational Fluid Dynamics the Finite Volume Method; Prentice Hall: Maldon, UK, 1995.
- 28. Roe, P.L. Characteristic-Based Schemes for the Euler Equations. Annu. Rev. Fluid Mech. 1986, 18, 337–365. [CrossRef]
- 29. Agarwal, R. Computational fluid dynamics of whole-body aircraft. Annu. Rev. Fluid Mech. 1999, 31, 125–169. [CrossRef]
- 30. Gisler, G.R. Tsunami Simulations. Annu. Rev. Fluid Mech. 2008, 40, 71–90. [CrossRef]
- 31. Pirozzoli, S. Numerical Methods for High-Speed Flows. Annu. Rev. Fluid Mech. 2011, 43, 163–194. [CrossRef]
- 32. Hirsch, C. Numerical computation of internal and external flows. In *Computational Methods for Inviscid and Viscous Flows*; Vrije Universiteit Brussel: Brussels, Belgium, 1990; Volume 2.
- 33. Karniadakis, G.E.; Sherwin, S. Spectral/hp Element Methods for CFD; Oxford University Press: New York, NY, USA, 1999.
- 34. Marsden, A.L. Optimization in Cardiovascular Modeling. Annu. Rev. Fluid Mech. 2014, 46, 519–546. [CrossRef]
- 35. Mavriplis, D.J. Unstructured grid techniques. Annu. Rev. Fluid Mech. 1997, 29, 473–514. [CrossRef]
- 36. Kirk, B.S.; Carey, G.F. Development and validation of a SUPG finite element scheme for the compressible Navier–Stokes equations using a modified inviscid flux discretization. *Int. J. Numer. Methods Fluids* **2008**, 57, 265–293. [CrossRef]
- 37. Catabriga, L.; Coutinho, A.L. Implicit SUPG solution of Euler equations using edge-based data structures. *Comput. Methods Appl. Mech. Eng.* **2002**, *191*, 3477–3490. [CrossRef]
- 38. Catabriga, L.; Coutinho, A.; Tezduyar, T.E. Finite element SUPG parameters computed from local dof-matrices for compressible flows. In Proceedings of the 24th Iberian Latin-American Congress on Computational Methods in Engineering, Ouro Preto, Brazil, 29–31 October 2003.
- 39. Catabriga, L.; Coutinho, A.L.; Tezduyar, T.E. Compressible flow SUPG stabilization parameters computed from degree-of-freedom submatrices. *Comput. Mech.* **2006**, *38*, 334–343. [CrossRef]
- 40. Hughes, T.J.; Mallet, M. A new finite element formulation for computational fluid dynamics: III. The generalized streamline operator for multidimensional advective-diffusive systems. *Comput. Methods Appl. Mech. Eng.* **1986**, *58*, 305–328. [CrossRef]
- 41. Tezduyar, T.E.; Senga, M. SUPG finite element computation of inviscid supersonic flows with YZβ shock-capturing. *Comput. Fluids* **2007**, *36*, 147–159. [CrossRef]
- 42. Jiang, B.n. *The Least-Squares Finite Element Method: Theory and Applications in Computational Fluid Dynamics and Electromagnetics;* Springer Science: New York, NY, USA, 2013.
- 43. Shakib, F.; Hughes, T.J.; Johan, Z. A new finite element formulation for computational fluid dynamics: X. The compressible Euler and Navier–Stokes equations. *Comput. Methods Appl. Mech. Eng.* **1991**, *89*, 141–219. [CrossRef]
- 44. Bova, S.; Bond, R.; Kirk, B. Stabilized finite element scheme for high speed flows with chemical non-equilibrium. In Proceedings of the 48th AIAA Aerospace Sciences Meeting Including the New Horizons Forum and Aerospace Exposition, Orlando, FL, USA, 4–7 January 2010; p. 1560.
- 45. Kirk, B.S. Adaptive Finite Element Simulation of Flow and Transport Applications on Parallel Computers. Ph.D. Thesis, The University of Texas at Austin, Austin, TX, USA, 2007.
- 46. Kirk, B.; Bova, S.; Bond, R. A Streamline-Upwind Petrov-Galerkin Finite Element Scheme for Non-Ionized Hypersonic Flows in Thermochemical Nonequilibrium. In Proceedings of the 49th AIAA Aerospace Sciences Meeting including the New Horizons Forum and Aerospace Exposition, Orlando, FL, USA, 4–7 January 2011; p. 134.

Fluids **2024**, 9, 18

47. Aliabadi, S.K. Parallel Finite Element Computations in Aerospace Applications. Ph.D. Thesis, University of Minnesota, Minneapolis, MN, USA, 1994.

- 48. Aliabadi, S.K.; Tezduyar, T.E. Parallel fluid dynamics computations in aerospace applications. *Int. J. Numer. Methods Fluids* **1995**, 21, 783–805. [CrossRef]
- 49. Le Beau, G.J. The Finite Element Computation of Compressible Flows. Ph.D. Thesis, University of Minnesota, Minneapolis, MN, USA, 1990.
- 50. Senga, M. Improved SUPG Formulations for Compressible Flows. Ph.D. Thesis, Rice University, Houston, TX, USA, 2006.
- 51. Bento, S.S.; Barbosa, P.W.; Santos, I.P.; de Lima, L.M.; Catabriga, L. A Nonlinear Finite Element Formulation Based on Multiscale Approach to Solve Compressible Euler Equations. In Proceedings of the International Conference on Computational Science and Its Applications, Trieste, Italy, 3–6 July 2017; pp. 735–743.
- 52. Bento, S.S.; de Lima, L.M.; Sedano, R.Z.; Catabriga, L.; Santos, I.P. A Nonlinear Multiscale Viscosity Method to Solve Compressible Flow Problems. In Proceedings of the 16th International Conference on Computational Science and Its Applications ICCSA 2016, Beijing, China, 4–7 July 2016; Proceedings, Part I; pp. 3–17.
- 53. Kovasznay, L. Laminar flow behind a two-dimensional grid. In *Mathematical Proceedings of the Cambridge Philosophical Society*; Cambridge University Press: Cambridge, UK, 1948; Volume 44, pp. 58–62.
- 54. Toro, E.F. *Riemann Solvers and Numerical Methods for Fluid Dynamics: A Practical Introduction;* Springer Science & Business Media: Heidelberg/Berlin, Germany, 2013.
- 55. Nazarov, M. An Adaptive Finite Element Method for the Compressible Euler Equations. Ph.D. Thesis, KTH, Stockholm, Sweden, 2009.
- 56. Chhunchha, A.C. Aerodynamic Heating Analysis of Re-Entry Space Capsule Using Computational Fluid Dynamics. Master's Thesis, California State University, Long Beach, CA, USA, 2018.

**Disclaimer/Publisher's Note:** The statements, opinions and data contained in all publications are solely those of the individual author(s) and contributor(s) and not of MDPI and/or the editor(s). MDPI and/or the editor(s) disclaim responsibility for any injury to people or property resulting from any ideas, methods, instructions or products referred to in the content.